30. Cosmic Rays

Revised March 2024 by J. Alvarez-Muñiz (Santiago de Compostela U.), Z. Cao (IHEP Beijing), U.F. Katz (Erlangen U.), P. Mertsch (TTK, RWTH) and C. Spiering (DESY, Zeuthen).

30.1 Theory

Cosmic rays (CRs) are a non-thermal population of particles that pervade the Universe. Their salient characteristics can be inferred from their major observational properties: spectrum, composition and arrival directions. For charged CRs, the energies extend from tens of MeV to close to 1 ZeV, the intensity is $\sim 10^4\,\mathrm{m^{-2}\,s^{-1}\,sr^{-1}}$ above 1 GeV, but the differential spectrum falls steeply with energy E, following a power-law dependence $E^{-\gamma}$. The most striking spectral features are the "knee" at a few PeV where the spectral index γ changes from ~ 2.7 to ~ 3, the "second knee" at ~ 100 PeV with a change to ~ 3.3 and the "ankle" at a few EeV where γ changes to ~ 2.5. The flux is largely suppressed above a few tens of EeV. (More detailed discussion of spectral features can be found below in Secs. 30.2.1 and 30.2.2.) Charged CRs are composed mostly of protons, helium, and other nuclei, as well as electrons, positrons and anti-protons. The arrival directions are mostly isotropic, but below and around the knee interesting $\mathcal{O}(10^{-4}\ldots10^{-3})$ anisotropies due to the distribution of sources and properties of the Galactic magnetic fields have been observed, reaching $\sim \mathcal{O}(10^{-1})$ at the highest energies. Gamma-rays can be resolved into those from astrophysical sources ($\sim$ 6660 [1] above 50 MeV, $\sim$ 300 [2, 3] at TeV energies), plus diffuse fluxes of galactic and extra-galactic origin, predominantly showing power-law dependence on energy. The observation of high-energy neutrinos has opened a new window; while the distribution is largely isotropic, evidence for two extra-galactic sources as well as for a contribution from the galactic plane has been found. The energy spectra of charged CRs, diffuse gamma-rays and neutrinos are shown in Fig. 30.1. Combined observations of charged CRs, gamma-rays and neutrinos as well as gravitational waves (see Sec. 21.2.3) allow for valuable insights into the most extreme astrophysical environments and is referred to as multi-messenger astrophysics. Adding the contribution from all species results in the all-particle spectrum. While it was believed for a long-time that it was a featureless power law up to the knee at a few PeV, it has now been recognized that it has much more structure, mirroring the features in the individual species. These features carry important information on the acceleration and transport of CRs.

The energy variables used are kinetic energy E, kinetic energy per nucleon, $E_\mathrm{n} = E/A$ for a particle of mass number A, or rigidity $\mathcal{R} \equiv pc/(Ze)$ (given in units of volt) for a particle of charge number Z, p being the momentum of the particle; the term rigidity refers to the resistance against deflections in a magnetic field B: particles of low (high) rigidity have small (large) gyroradii $r_\mathrm{g} = \mathcal{R}/B$. Kinetic energy is closely related to the experimental signatures of a calorimetric instrument, while rigidity is the most natural one for a spectrometric one. Note also that relativistic nuclei suffer little energy losses and their transport is prescribed by magnetic fields, thus it can only depend on rigidity. The *intensity* J of CRs, also called the diffuse flux, is defined through the differential number $\mathrm{d}N$ of particles with energy in the interval $[E, E + \mathrm{d}E]$, crossing the area $\mathrm{d}A$ from a solid angle $\mathrm{d}\Omega$ in the time $\mathrm{d}t$: $\mathrm{d}N = J\,\mathrm{d}E\,\mathrm{d}A\,\mathrm{d}\Omega\,\mathrm{d}t$. Its isotropic part is related to the differential density $\psi = (4\pi/v)J$, v being the particle speed and to the phase-space density f as $J = p^2 f$. Note that the intensity can be also defined in reference to particle energy per nucleon or rigidity. To stress this, often the intensity is written as $\mathrm{d}J/\mathrm{d}E$, $\mathrm{d}J/\mathrm{d}E_\mathrm{n}$ or $\mathrm{d}J/\mathrm{d}\mathcal{R}$.

In the detection of CRs, two classes of techniques are distinguished [4]. *Direct observations*, see Sec. 30.2.1, make use of the interactions of CRs in particle physics detectors (e.g. trackers, spectrometers and calorimeters). Given the limited exposures of such instruments and the steeply falling spectra, this is currently only realistic below ~ 100 TeV. In *indirect observations*, see Sec. 30.2.2,

showers of secondary particles initiated by charged CR interactions in natural materials (e.g. air, water or ice) are detected through fluorescence, air-Cherenkov, water-Cherenkov or scintillation effects. This allows for large instrumented surfaces or volumes. Historically, the two classes of techniques have been employed by two separate communities and we structure the review of charged CRs accordingly. For detection of gamma-rays, direct observations are relevant mostly below hundreds of GeV; for gamma-rays of higher energies and neutrinos of essentially all energies, indirect observations are required.

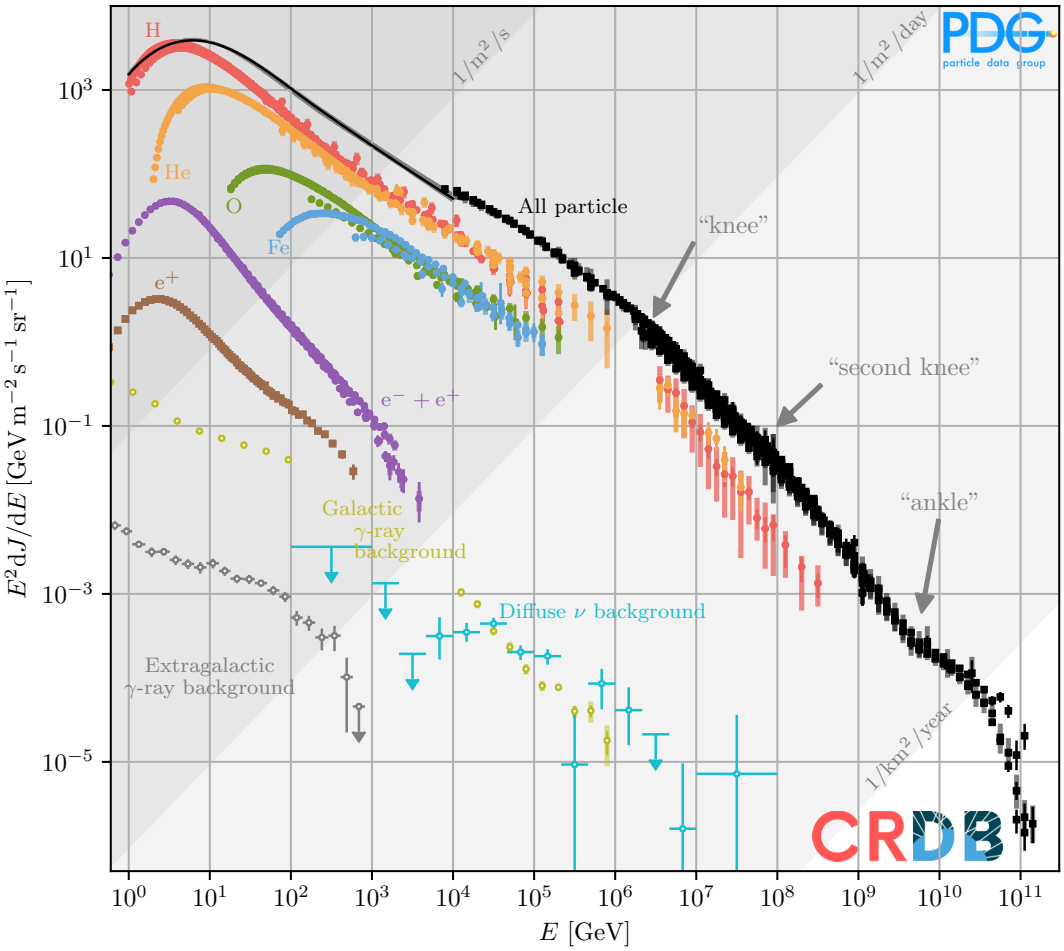

Figure 30.1: The spectrum of cosmic rays (CRs). Shown are measurements of the intensity of charged and neutral CRs, multiplied by kinetic energy squared. The data for the charged CRs [5–34] have been extracted from the Cosmic Ray Database (CRDB) [35]. Below 10^4 GeV, the all-particle spectrum is the sum of spline fits of the most important nuclear species. The diffuse γ-ray fluxes have been extracted from Refs. [36–38], measurements of the diffuse neutrino background from Ref. [39]. Energy-integrated intensities are indicated by the various diagonal lines.

Charged CRs are deflected by magnetic fields and so generally speaking the observed events do not point back to sources. CRs can however reach the earth from galactic and even cosmological distances. Between hundreds of MeV and at least a few PeV, CRs are believed to be of galactic origin; above a few EeV, the sources are most likely extra-galactic. If CRs with energies in excess of ~ 1 EeV came from sources in the Galactic disk, the angular distribution at Earth would be very

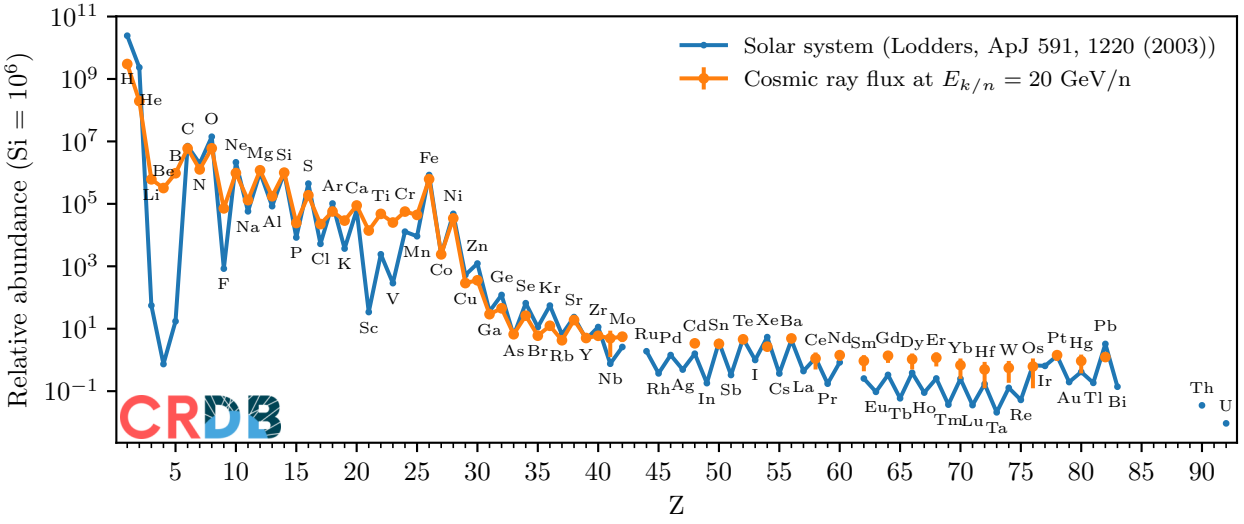

Figure 30.2: CR abundances compared with solar system ones [58]. Modified from [35].

anisotropic, which is at variance with observations. And if CRs below ~ 1 PeV were dominantly of extra-galactic origin, this would result in a gamma-ray flux from objects like the Large Magellanic Cloud exceeding observations [40]. Direct and indirect observations therefore also largely refer to galactic/extra-galactic sources, respectively. CRs with energies in excess of 1 EeV are referred to as ultra-high energy cosmic rays (UHECRs).

Sources of non-thermal electromagnetic radiation are routinely observed, see Sec. 30.3, yet the dominant source of locally measured CRs have not been unambiguously identified. Source candidates are typically associated with endpoints of stellar evolution or supermassive black holes that release large amounts of gravitational or rotational energy [41]. In the Galaxy, the prime candidates are supernova remnants [42] where particles can be shock-accelerated by their blast waves [43]. Other candidates are star cluster winds [44,45], stellar wind binaries, micro quasars [46] (a source powered by accretion from a donor star onto a stellar mass black hole) or even the Galactic Center [47]. The candidate sources for extra-galactic CRs are Active Galactic Nuclei (AGN) [48], specifically blazars and radio galaxies, gamma-ray bursts [49], starburst galaxies [50,51], pulsars [52] and magnetars [53]. These objects exhibit power-law spectra in electromagnetic radiation, albeit in limited wavelength ranges. The acceleration mechanisms considered in the literature are shock acceleration [43], stochastic acceleration [54], and reconnection [55]. A fundamental constraint on the maximum energy, the so-called Hillas criterion [56], follows from the requirement that the gyroradius must be smaller than the source size.

In the Milky Way, the dominant process in CR transport is diffusion as evidenced by the small anisotropies in CR arrival directions and by certain abundance ratios of nuclear species. This diffusive transport bears some resemblance with heat transport in that it smooths the spatial distribution of CRs. However, in contrast to heat transport, CR diffusion is not due to collisions, but interactions with turbulent magnetic fields. Generally, CRs interact "resonantly" with plasma waves, that is they get affected only by waves with a wavelength similar to the gyroradius of the CR particle. If this condition is satisfied, a CR particle will be deflected by the Lorentz force. Many random deflections lead to a random walk in space, that is diffusion [57].

There is a number of other processes contributing to the transport of charged CRs: momentum losses, i.e. radiative losses for electrons and positrons [59], ionization and Coulomb losses for nuclei,

electrons and positrons [60]; spallation, that is production of (mostly) lighter nuclei by inelastic collisions of heavier ones; and other inelastic collisions, e.g. the production of light mesons. We note that progress in the study of CR transport is often limited by the nuclear interactions since many cross-sections are poorly known, if at all [61]. The various processes are encoded in the CR transport equation [62], also referred to as the Parker transport equation [63] in the space physics community. This partial differential equation is supplemented by the boundary condition of free escape on the surface of the (often cylindrical) confinement volume. Only in simplified cases can this equation be solved analytically. The most instructive case is the 1D approximation where only the direction perpendicular to the Galactic disk is retained. The solution differs for *primaries*, that is species present and accelerated in the CR sources, and *secondaries*, which are not present in CR sources, but produced by inelastic collisions of primaries in the gaseous disk of the Galaxy. Diffusion in the Galaxy, characterized by a diffusion coefficient $\kappa(\mathcal{R})$, modifies the source spectrum $q(\mathcal{R})$, resulting in the steady-state spectrum $\psi(\mathcal{R}) \propto q(\mathcal{R})/\kappa(\mathcal{R})$. As the production spectrum of secondaries follows the steady-state spectrum of primaries, $q_2(\mathcal{R}) \propto \psi_1(\mathcal{R})$, the secondary steady-state spectrum is $\psi_2(\mathcal{R}) \propto q_2(\mathcal{R})/\kappa(\mathcal{R}) \propto \psi_1(\mathcal{R})/\kappa(\mathcal{R})$. As $\kappa(\mathcal{R})$ grows with $\mathcal{R}$, secondary spectra $\psi_2(\mathcal{R})$ fall more quickly with rigidity than primary spectra $\psi_1(\mathcal{R})$. Unstable secondaries provide additional constraints on the gas density and residence time of CRs. The solution of the transport equation in more realistic setups requires numerical codes [64–67].

Protons (iron nuclei) with energies in excess of $\sim 1\,\mathrm{EeV}$ ($\sim 26\,\mathrm{EeV}$) in a micro-Gauss magnetic field have gyroradii larger than the typical kiloparsec scales of the Galaxy, thus they cannot be confined. Their directions are however affected by so-called small-angle scattering, both in the Milky Way and possibly outside. As far as their spectrum and composition is concerned, protons and heavier nuclei suffer from inelastic collisions with the CMB and the extra-galactic background light at the highest energies. For protons above 10 EeV, photo-pion production limits the propagation distances to $\sim 100\,\mathrm{Mpc}$; for nuclei, heavier ones photo-disintegrate to lighter ones, also limiting their spatial reach. Both processes can lead to a suppression of the flux known as the GZK effect [68,69] and produce secondary gamma-rays and neutrinos. Other secondary particles include neutral and charged pions, which ultimately decay to photons, electrons, positrons and neutrinos, and electron-positron pairs which can also initiate a cascade of photons and lower energy electrons and positrons. The stable decay products, in particular gamma-rays and neutrinos can be used as an additional diagnostic tool for the study of the origin and transport of UHECRs.

In many astrophysical environments, the energy density of CRs constitutes a significant fraction of the total or is comparable to that of other ingredients. For instance, on galactic scales, the CR energy density is of the same order as that of magnetic fields, radiation fields or the turbulent gas. Due to their pressure, CRs can be dynamically important and shape their environments: Specifically, CRs contribute to the gravitational support of galaxies and can drive galaxy-scale outflows. They ionize neutral gas, thus determining coupling of gas and magnetic fields. CRs can generate turbulence by a variety of streaming instabilities [70, 71], which play a central role in shock acceleration and galactic transport [72]. Finally, CRs also produce diffuse emission through interactions with gas and radiation fields, an additional handle for CR studies.

CRs are also important probes of fundamental physics. If dark matter has interactions with the Standard Model, the products of self-annihilation or decay of DM particles can potentially be observed (DM, see Sec. 27.7). This is called DM indirect observation. Generically, one would expect similar rates of production of particles and antiparticles whereas astrophysical sources predominantly accelerate matter particles. It is therefore advisable to search for signals in CRs positrons, anti-protons and anti-nuclei [73, 74]. In fact, excesses have been reported of positrons and anti-protons, yet astrophysical pollutions and/or experimental systematic uncertainties can not be excluded. There have also been searches in gamma-rays and neutrinos and a number of studies have

indentified an excess of gamma-rays from the Galactic Center that is compatible with DM particles of weak-scale mass and weak annihilation cross-section [75]. Another target for exotic searches in CRs is anti-matter of primordial origin [76]. Most interestingly, the AMS-02 collaboration has claimed $\mathcal{O}(10)$ $\overline{\text{He}}$ candidate events, but whether those are of primordial origin as opposed to instrumental effects is at this point not clear.

30.2 Charged cosmic rays

30.2.1 *Direct observations*

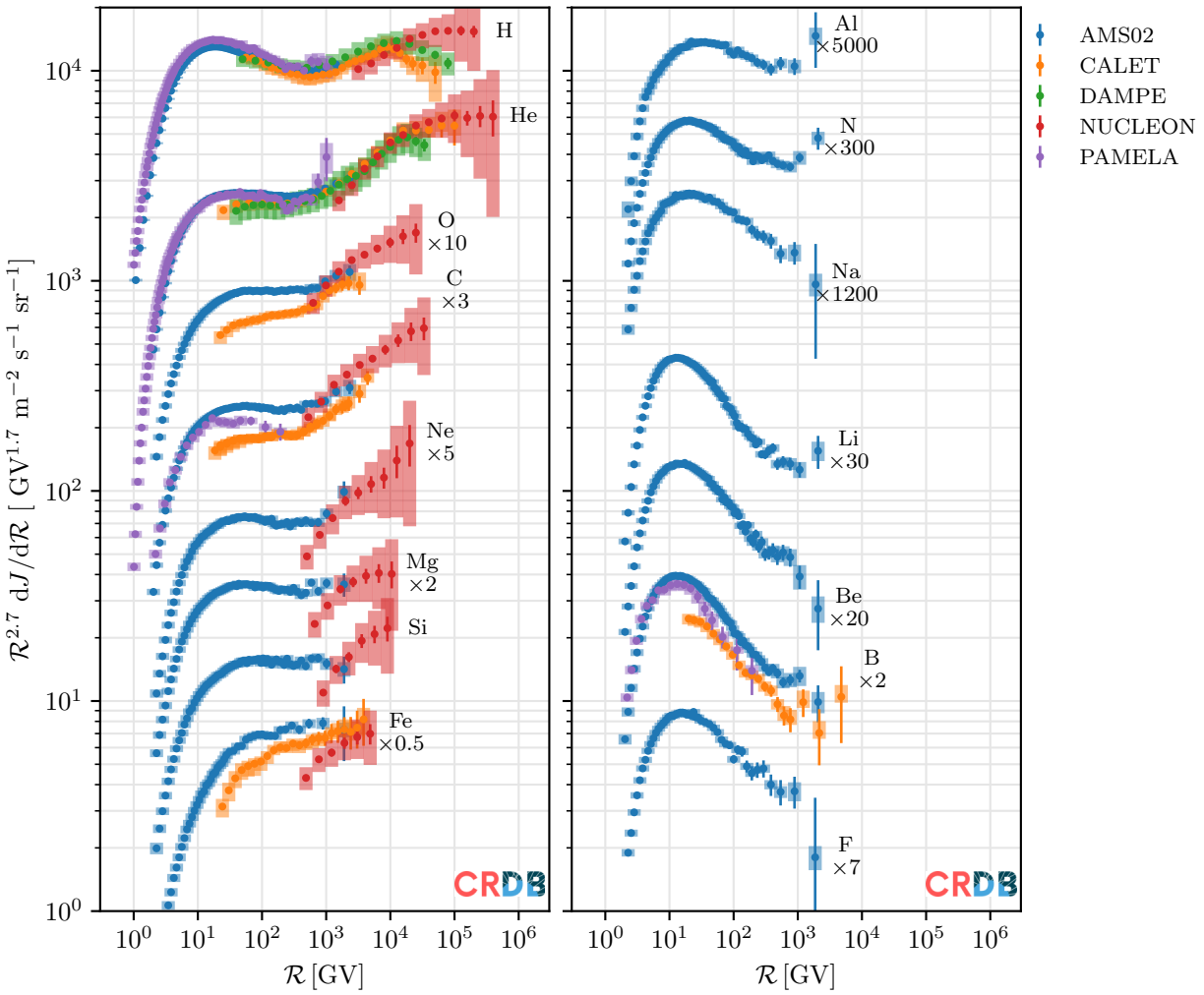

Figure 30.3: Rigidity spectra for a selection of CR nuclei. Primary species are shown in the left panel, (mostly) secondary species in the right panel. The error bars denote the statistical uncertainties, the shaded bars represent the systematic uncertainties. The spectra have been shifted and multiplied by $\mathcal{R}^{2.7}$ to better bring out spectral features. Here, we have constrained ourselves to data from space-borne experiments of the last ten years, that is AMS-02 [12, 19, 77–79], CALET [14, 20, 80, 81], DAMPE [11, 17], NUCLEON [9] and PAMELA [6, 82]. Data have been extracted from [35].

Direct observations [83] cover energies between a few MeV and a few tens of TeV, where CRs must be of Galactic origin. At energies lower than a few MeV, solar energetic particles [84] are

dominating the flux; above a few tens of TeV, the fluxes are too low to be observed directly and instead indirect detection techniques [85] need to be used. Besides spectral information, direct observations enable identification of species on an event-by-event basis, certain experiments even provide isotopic discrimination. We present a compilation of direct observations of the most important primary and secondary nuclei in Fig. 30.3. These show broken power-law spectra in rigidity with $J \propto E^{-\gamma}$ in different rigidity ranges. The various changes in spectral slope contain valuable information on the rigidity-dependence of the diffusion coefficient κ and the primary source spectra q_1.

Protons are dominating the CR flux by number and by energy below $\sim$ 10 TeV and their spectrum has been measured with excellent precision. Measurements of the proton spectrum and other primaries are shown in the left panel of Fig. 30.3. Data from the AMS-02 experiment [12] show a $\mathcal{R}^{-2.8}$ spectrum above $\sim$ 10 GeV with a break to $\mathcal{R}^{-2.7}$ at $\sim$ 300 GV. This feature had been observed by PAMELA earlier [6], and also with CREAM and ATIC for heavier nuclei [86, 87]. As a reminder, at energies above a few GeV, the measured spectrum can be interpreted as the ratio of the source spectrum $q(\mathcal{R}) \propto \mathcal{R}^{-\Gamma}$ divided by the diffusion coefficient $\kappa(\mathcal{R}) \propto \mathcal{R}^{\delta}$. Thus a spectral index of $\gamma = \Gamma + \delta \simeq 2.8$ can describe the data. On the basis of proton data alone, the degeneracy between the source spectral index Γ and the spectral index of the diffusion coefficient δ cannot be broken. Also, the break at $\sim$ 300 GV could be a break in the source spectrum or in the diffusion coefficient, but see below. At energies lower than $\sim$ 10 GeV, the spectrum turns over because of energy losses and solar modulation. At energies beyond the reach of AMS-02, both DAMPE and CALET data show a softening at rigidity $\sim$ 10 TV [11, 14], confirming earlier indications [86, 87].

Most of the other primary species, that is helium, carbon, nitrogen, oxygen, neon, magnesium and silicon with the notable exception of iron, also show a spectral break at $\sim$ 300 GV, but their spectra are generally harder than the proton one, e.g. $\gamma_{\rm He} < \gamma_{\rm p}$, both below and above the break. Suggested explanations for this difference in spectrum include gradients in the relative circumstellar abundances of protons and heavier nuclei or invoking different source populations for these two groups. At $\sim$ 10 TV a softening break mirrors the feature observed in protons [80]. Above an energy of $\sim$ 100 TeV, elemental information is scarse, but a combined analysis of proton and helium by DAMPE extends to $\sim$ 300 TeV and indicates another spectral hardening [88]. (Note that this data are not included in Fig. 30.3 though.) Such a feature was to be expected to a certain degree in order to connect to the indirect measurements of proton and helium which start at $\sim$ 1 PeV. Note that there exist some 20 % discrepancies between the oxygen and carbon data from AMS-02 [12], CALET [17] and PAMELA experiments [82] in normalization, possibly also in spectral shapes.

Iron constitutes an exception to the otherwise rather similar slopes of primary species heavier than proton. As is also the case for other nuclei, AMS-02 [19] and CALET [20] disagree on the normalization by $\sim$ 20 %, but both measurements of the iron spectrum exhibit spectral shapes different from the oxygen ones. While the ratio of Fe/O could be accommodated if all nuclei traversed the same amount of matter (grammage) between source and observer (the so-called slab model), more realistic models cannot explain the observations [89]. Also, the AMS-02 data on Fe/O are in tension with earlier measurements [90, 91]. Most interestingly, if extrapolated to lower energies, the Fe/O could only be accommodated if solar modulation was negligible.

Measurements of *stable* secondary nuclei contribute two important pieces of information to the standard scenario of galactic CRs: First, their over-abundance in CRs (with respect to solar system values, see Fig. 30.2) indicates diffusion as the primary transport process; and second, their spectral shapes, or rather the difference in spectral shapes between secondaries and primaries allows inference of the diffusion coefficient. Specifically, at energies where energy losses can be ignored for nuclei, that is above a few GeV, the propagated spectra of primaries $\psi_1(\mathcal{R})$ are approximately $\propto \mathcal{R}^{-2.8\ldots-2.7}$, which is explained as a softening of the sources spectrum $q_1(\mathcal{R})$. Secondaries, however,

are produced with a spectrum proportional to the propagated primary spectrum, $q_2(\mathcal{R}) \propto \psi_1(\mathcal{R})$ which also gets further softened by the diffusion coefficient. The difference in spectral index can be clearly seen when comparing primary with secondary spectra. A compilation of such secondary spectra from AMS-02 [12, 78, 79], CALET [81] and PAMELA [82] is shown in the right panel of Fig. 30.3. Lithium, beryllium, boron and fluorine can be identified as almost pure secondaries by their soft spectra. Aluminium, sodium and neon, however, have harder spectra, somewhere intermediate between primaries and secondaries. This can be understood as being due to mixture of softer secondary contribution from spallation in the interstellar medium (ISM) and a harder primary source component. Secondaries also exhibit a hardening break at $\sim$ 300 GV, but the change in spectral slope is about twice as big [92] when compared to that of the primaries. This fact serves as evidence for the break being due to a change in the rigidity-dependence of the diffusion coefficient, as opposed to a break in the source spectrum [93, 94]. Recently, there have been some claims of excesses in low-energy intensities of Li, F, Al [95], however these claims are somewhat controversial. We note the importance of composition studies for shedding light on cosmic ray origin.

Unstable isotopes with a lifetime similar to the residence time of CRs can be used to study galactic propagation. Among these species, ^{10}Be, ^{26}Al and ^{60}Fe have been studied the most as their rest lifetime is close to the residence time of CRs at GV rigidities. Roughly speaking, the flux ratio of an unstable and a stable secondary that are both produced from similar primary species, reflects the ratio of production cross-section at high energies (where decay is suppressed by time-dilation). On the other hand, at low energies, this ratio is suppressed due to the decay of the unstable species. The transition takes place at energies where the decay time equals the residence time in the Galactic disk. At present, there is limited information on ratios at energies beyond 1 GeV/nucleon where the transition for the ratios of the above mentioned unstable nuclei is expected to take place.

CR electrons are also believed to be accelerated in the preferred candidate sources of nuclei, that is, SNRs. Other source candidates are pulsars and pulsar wind nebulae (PWNe); in the simplest models those also accelerate similar amounts of CR positrons. We show a compilation of the most recent and precise data from AMS-02 [12], CALET [23], DAMPE [21], *Fermi*-LAT [22], H.E.S.S. [96] and PAMELA [97] on CR electrons, positrons and the sum of electrons and positrons in Fig. 30.4. In addition to the processes at work in the propagation of nuclei, electrons suffer significant radiative losses due to synchrotron emission and inverse Compton scattering. In fact, for the parameters determined in the standard scenario, the cooling time is shorter than the residence time above $\sim$ 10 GeV. For the same source spectral index, the spectra are predicted to be softer than those of primary nuclei. Indeed, the observed spectrum is roughly $\propto E^{-3.1}$.

If positrons were only produced by spallation in the interstellar medium, the positron spectrum should be softer than the electron one, however, on the contrary it is markedly harder. Between $\sim$ 10 GeV and $\sim$ 100 GeV its spectral index γ_{e^+} transitions from 3 to 2.7 before a spectral break or cut-off at a few hundred GeV as shown in Fig. 30.4. The fact that the positron spectrum is harder than the electron one above a few GeV had first been detected by PAMELA [98] after earlier indications. AMS-02 has now measured the spectrum with great precision up to $\sim$ 1 TeV [12]. The origin of the harder positron spectrum remains unclear today. After the discovery by PAMELA, there had been hope that this was the long sought for signature of self-annihilation or decay of weakly interacting massive particles (WIMP) dark matter [99]. However, such interpretations are now severely constrained by observations of gamma-rays, anti-protons and the cosmic microwave background (CMB, see Chap. 29). Production of e^+ in pulsars or PWNe is an astrophysical explanation that had been hypothesized long before the PAMELA observations (e.g. [100]). Recently, there have been observations of extended emission of high-energy gamma-rays, so-called gamma-ray halos around PWNe [101], interpreted as evidence of the presence of high-energy electrons and positrons around these objects. Other astrophysical explanations include the production and

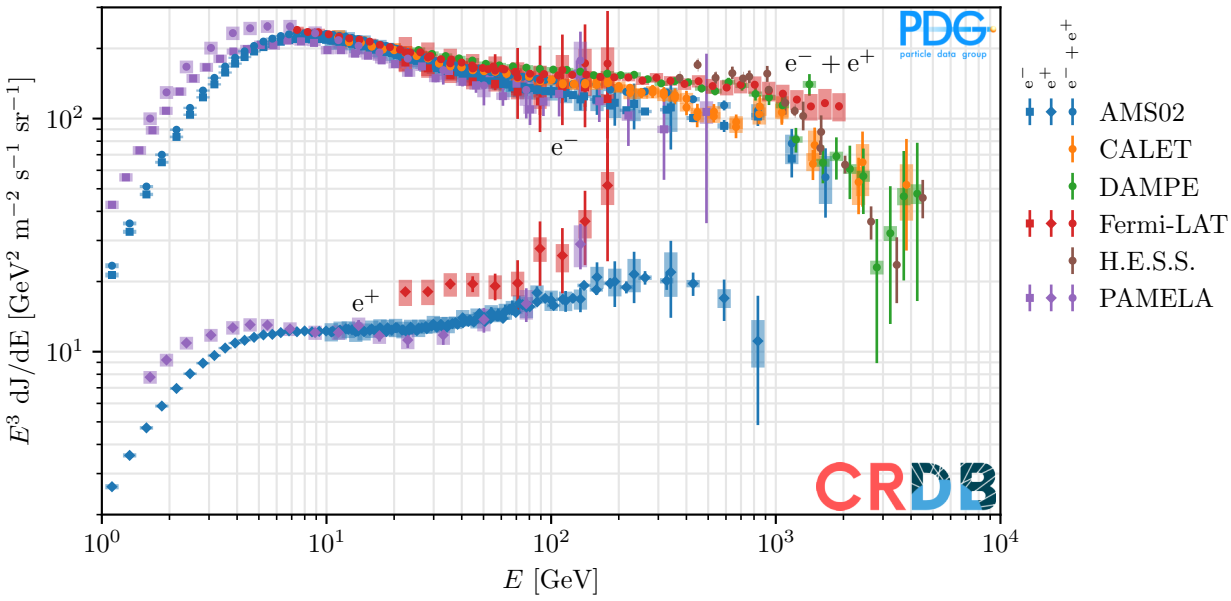

Figure 30.4: Intensities of cosmic ray electrons (squares), positrons (diamonds) and their sum (dots) as a function of kinetic energy E. We have included data from the most recent space experiments AMS-02 [12], CALET [23], DAMPE [21], *Fermi*-LAT [22] and PAMELA [97] as well as from the ground-based H.E.S.S. experiment [96]. The spectra have been multiplied by E^3 to enhance the visibility of the spectral features. Data have been extracted from [35].

subsequent acceleration of secondaries in old SNRs [102, 103].

Measurements of the spectra of electrons and positrons are particularly interesting at high energies. Due to the increasingly important radiative losses, the distance to the sources which could significantly contribute to the total flux decreases with energy. Estimates at 1 TeV of this diffusion-loss length are only $\simeq 0.3$ kpc. The predicted spectrum therefore becomes rather sensitive to the exact distances and ages of young, nearby sources which manifest as individual bumps in the spectrum. Turning this around, observations can be used to search for young, nearby sources of CRs. At energies above ~ 1 TeV, only calorimetric observations are currently available which cannot discriminate between electrons and positrons. Observations of the all-electron flux, that is the sum of electron and positron fluxes, find a break at ~ 1 TeV, displayed in Fig. 30.4. This was first seen by H.E.S.S. [96] and later confirmed by DAMPE [21] and CALET [23]. The break by about one power in energy has been interpreted either as due to a break in the spectrum of a large number of sources, e.g. [104] or as a stochasticity effect from a small population of sources [105].

In the standard scenario of galactic cosmic rays, anti-protons are also produced as secondary particles, but unlike secondary nuclei or electrons and positrons, their production is kinematically suppressed at lower energies. The spectrum of anti-protons observed by PAMELA (Fig. 3 in [106]) and AMS-02 (Fig. 62 in [12]) is close to $E^{-2.8}$, which is somewhat harder than predicted by earlier models. More recent models can accommodate the observations, in part due to a re-evaluation of the production cross-section. Note that there have been claims that the transport parameters obtained when fitting to proton and anti-proton data differ from those obtained by fitting to heavier nuclei [107]. An alternative explanation for the harder anti-proton spectrum is the acceleration of secondaries in old supernova remnants [103, 108]. At energies of a few GeV, there have been claims of an excess in the measured anti-proton spectrum. If interpreted as a sign of dark matter

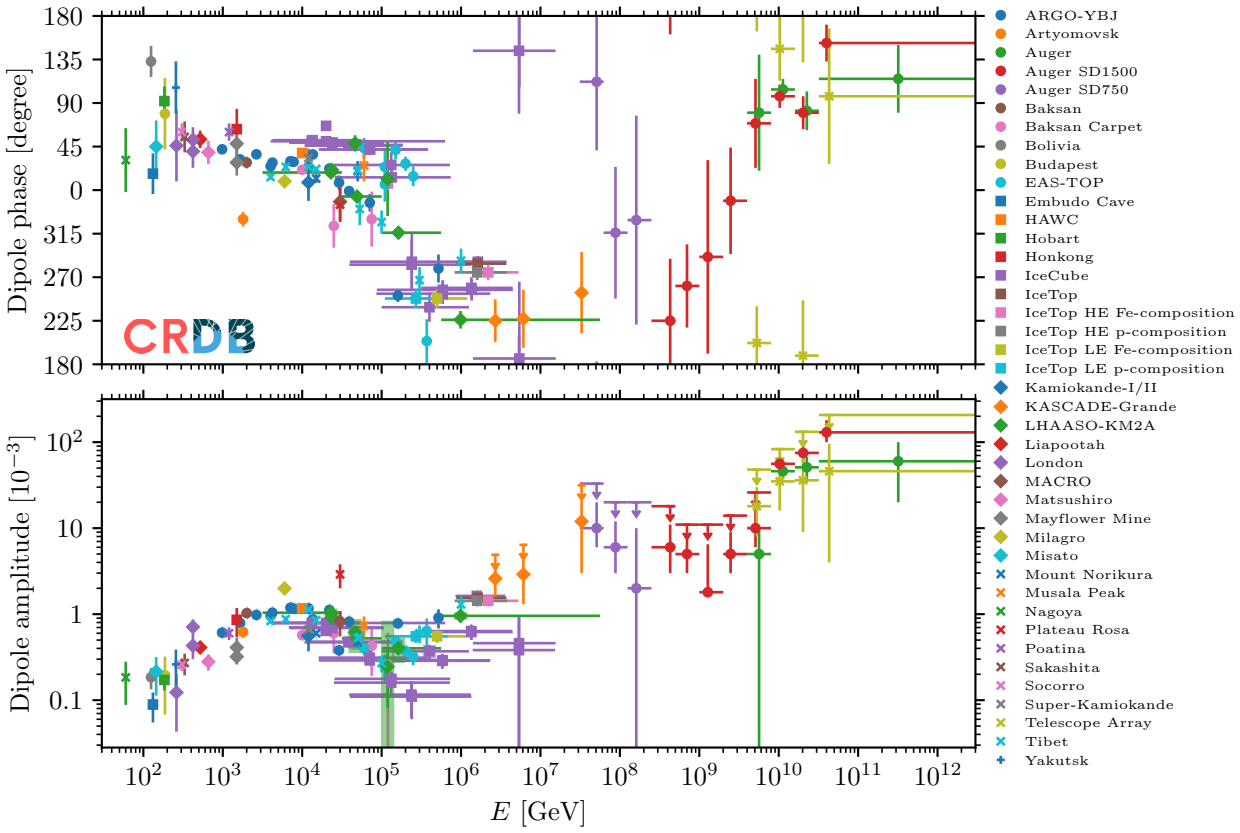

Figure 30.5: Phase and amplitude of the dipole anisotropy in CRs. Modified from Ref. [35].

annihilation, such an excess could be explained by a weak-scale particle of mass of a few tens of GeV and annihilation cross-sections close to the thermal relic value. However, the significance of the signal is relatively low if correlations in the cross-section uncertainties and in the measurements are taken into account. Considering the spectra of anti-protons together with protons and positrons, it appears that all three have similar spectral indices between $\sim 10\,\mathrm{GV}$ and $\sim 300\,\mathrm{GV}$. This is rather surprising, given that as secondaries positrons and anti-protons should have spectra softer than the primary protons, due to energy losses and diffusive losses, respectively. In the standard scenario this cannot be explained and thus must be considered a mere coincidence.

The only astrophysical mechanism for production of anti-nuclei like anti-deuterons ($\overline{\mathrm{D}}$) or anti-helium ($^3\overline{\mathrm{He}}$ or $^4\overline{\mathrm{He}}$) is coalescence of anti-nucleons produced in the spallation of primary nuclei in the interstellar medium. Due to kinematics, however, this is significantly suppressed at energies below a few GeV, thus rendering this an interesting channel for searches of dark matter, in particular for relatively light WIMPs with masses of a few GeV or less. The AMS-02 collaboration has reported some ten candidate events of anti-helium, yet the rate of $^3\overline{\mathrm{He}}$ or $^4\overline{\mathrm{He}}$ is incompatible with models of coalescence (e.g. [109]). Currently, the most constraining limits on $\overline{\mathrm{D}}$ are from the BESS balloon flights [110]. This should be improved on by the upcoming GAPS experiment, and also an upgrade of the AMS-02 experiment increasing the acceptance by a factor of three could help clarifying the situation.

Another important observable in the study of CRs are anisotropies, most commonly defined as the relative directional deviation of the CR intensity from the angular average. As the typical

anisotropies are at the level of one part in 10^3 or 10^4, high statistics are required. At TeV and PeV energies, only ground-based experiments have enough statistics, yet they cannot constrain the component of the anisotropy that is aligned with the Earth's rotation axis. Traditionally, therefore, only the projection of the true 2D dipole into the equatorial plane has been reported in terms of an amplitude and phase. We show a compilation [35] in Fig. 30.5. The amplitude is at the level of $\simeq 10^{-4}$ at energies of hundreds of GeV and increases to $\simeq 10^{-3}$ at tens of TeV. At ~ 100 TeV there is a dip before the amplitude rises again. Beyond a few PeV upper limits exist at the level of 10^{-2}. The Compton-Getting effect [111,112], that is a dipole anisotropy due to the relative motion of the solar system with respect to the Galactic rest frame has been experimentally confirmed [113]. The phase is relatively constant at a direction of 45° and switches to 250°, which is close to the Galactic Center direction, also around 100 TeV. For a description of anisotropies at the highest energies see Section 30.2.2. In addition, observations of anisotropies on scales smaller than the dipole have been reported (see Ref. [114]). These are not expected in standard diffusion theories that only predict a dipole. The leading explanation is the generation due to the specific realization of the turbulent magnetic field in our Galactic neighbourhood.

30.2.2 *Indirect observations*

In the energy range above $\simeq 1$ PeV the intensity of cosmic rays is so low that it prevents the collection of a statistically significant sample of these particles in a direct manner with detectors carried on balloons or satellites. Instead, cosmic rays are detected indirectly through the cascade of particles they produce in the atmosphere, the so-called extensive air showers (EAS). In this way, cosmic rays up to and even above 100 EeV have been observed [115,116], corresponding to about a hundred million times larger energy than that achieved by particles accelerated in human-made experiments.

Extensive Air Showers. Extensive air showers (EAS) are cascades of millions to billions of secondary particles initiated by a single primary particle (cosmic ray: proton, neutron or heavier nucleus; photon; or neutrino) of energy E in the atmosphere. Due to the small density of air $\rho \lesssim 10^{-3}\,\mathrm{g\,cm^{-3}}$, the shower develops throughout the whole of the atmosphere, and for a primary particle of 10 EeV has a lateral spread of $\sim 10\,\mathrm{km}^2$ at ground level, hence the name EAS.

When an energetic, $E \gtrsim 1$ PeV, cosmic proton or nucleus interacts with a nucleus of air, it generates between a few and hundreds of secondary particles depending on its energy. On average $\sim 30\% - 40\%$ of the energy of the primary particle is carried by a leading baryon or nucleus. The remaining energy is employed in the creation of ultra-relativistic secondary particles, most of them charged ($\pi^\pm$) and neutral (π^0) pions, with a smaller number of hadrons and heavier mesons such as charged and neutral kaons, ρ-mesons, etc. The energy of the primary particle rapidly degrades into a large number of secondaries that can subsequently interact or decay depending on the nature and energy of the particle and the density of the medium, further contributing to the shower development. If $\pi^\pm$ live long enough they can interact with an air nucleus before decaying. At altitudes of a few km where the atmosphere is less dense than at sea level, most $\pi^\pm$ with $E_{\pi^\pm} \gtrsim 100$ GeV interact while lower energy $\pi^\pm$ decay. Interacting $\pi^\pm$ along with the leading baryon and other hadrons, form a penetrating core of shower particles constituting the *hadronic component* of the cascade (Fig. 30.6). Charged pions decaying into muons, $\pi^+ \to \mu^+ + \nu_\mu$ and $\pi^- \to \mu^- + \bar{\nu}_\mu$, represent the main contribution to the *muonic component* of the shower (Fig. 30.6), being also responsible for the production of the bulk of the so-called atmospheric neutrinos. Most muons of energies above a few GeV travel through the atmosphere without decaying and reach ground, constituting a penetrating component of the shower. On the other hand, most π^0s, continuously produced in the hadronic core of the shower, do not travel long enough distances to interact with an air nucleus unless their energy

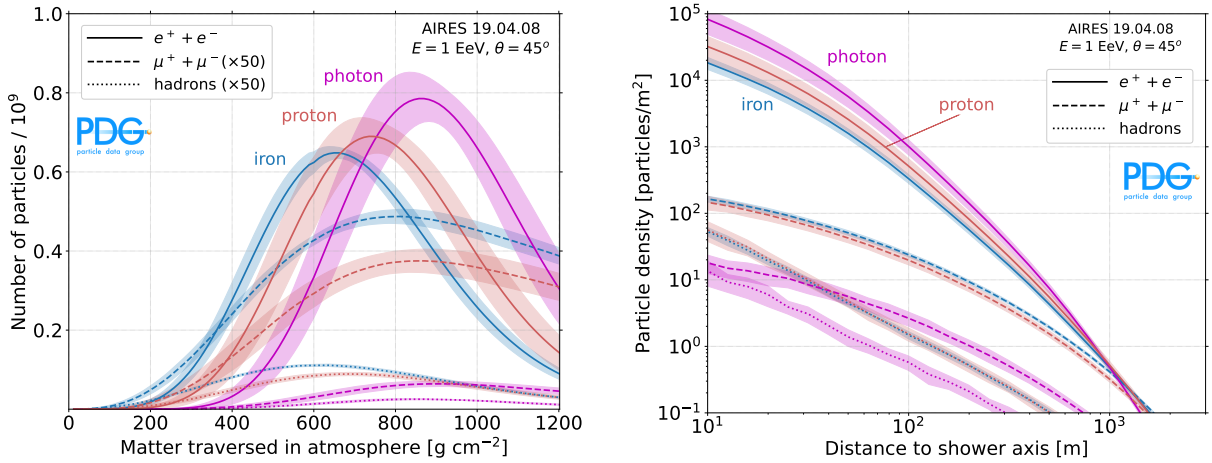

Figure 30.6: Left: Average number of $e^+ + e^-$, $\mu^+ + \mu^-$, and hadrons (lines), and their $\pm 1\,\sigma$ deviation (bands), as a function of matter (in $\mathrm{g\,cm^{-2}}$) crossed in the atmosphere along the shower axis. The profiles are obtained with AIRES simulations [117] of proton, iron and photon-induced extensive air showers of energy $E = 1\,\mathrm{EeV} = 10^{18}\,\mathrm{eV}$ and zenith angle $\theta = 45°$ w.r.t. the vertical to ground (at depth $870\,\mathrm{g\,cm^{-2}}$). Right: Lateral development (perpendicular to shower axis) at ground level of the same components as in the left panel as a function of distance to shower axis.

is well above 1 EeV. Instead, they decay almost immediately $\pi^0 \to \gamma\gamma$, initiating electromagnetic showers. Neutral pions play a significant role in generating the *electromagnetic component* that forms the majority of the shower (Fig. 30.6). This is composed of e^- and e^+ with a mean energy of 10 MeV as a result of photon pair production, as well as secondary photons from bremsstrahlung. Decaying muons also contribute to the electromagnetic component of the shower. The longitudinal development of the distinct and intertwined shower components, electromagnetic, muonic, and hadronic, is shown in Fig. 30.6. High-energy primary or secondary photons can occasionally photoproduce $\pi^\pm$ and initiate a hadronic subcascade resulting in an additional muonic component.

As a cosmic ray shower develops in the atmosphere, the number of particles increases in the longitudinal direction along the shower axis. The amount of matter traversed, X, is measured in units of $\mathrm{g\,cm^{-2}}$. The shower reaches a maximum size of the electromagnetic component $N_{\max}$ at a depth known as $X_{\max}$ (Fig. 30.6). The number of electrons and positrons declines rapidly after maximum when their energy reaches the *critical energy* in air, $\sim 80\,\mathrm{MeV}$, and they lose their remaining energy dominantly through ionization loss. Since neutrinos do not suffer electromagnetic interactions, and high energy muons reach ground level after releasing only a portion of their energy, a fraction of the energy of the primary initiating the shower is not deposited in the atmosphere. This is the so-called *invisible energy* that amounts to $\approx 10\% - 20\%$ of the shower energy for energies above 0.1 EeV, decreasing with the energy of the primary particle initiating the shower and increasing with its mass number [118]. At the same time the shower develops in the transverse or lateral dimension to the shower axis, as shown in Fig. 30.6, mainly due to the transverse momentum in hadronic interactions and multiple Coulomb scattering of e^- and e^+.

Shower development is driven by the particles carrying most of the energy in the forward region of the kinematical phase space of the collisions with air nuclei. Particle production is dominated by non-perturbative QCD which is necessarily treated by using phenomenological approaches. Moreover, particle collisions occurring in the atmosphere at 0.1 EeV are equivalent to center-of-mass

energies presently achieved at the LHC, and this energy scales up by a factor of approximately 30 at the highest cosmic ray energies observed. These two facts result in the need for extrapolations both in energy and phase space when modeling hadronic interactions. The cosmic-ray community has developed sophisticated simulation packages such as AIRES [117] and CORSIKA [119] to predict EAS observables as a function of primary energy and mass. These programs adopt models of hadronic interactions such as SIBYLL [120], QGSJET [121] and EPOS [122], tuned to a large data set including recent LHC data. Inferring fundamental properties of the primary particle initiating the shower, most notably its mass, requires the use of these air shower simulations. Large uncertainties remain, both due to theoretical limitations and the lack of data from existing collider experiments. A toy model to describe electromagnetic showers is due to Heitler [123], while for hadronic showers a model was developed by Matthews [124]. These oversimplified models shed light on the relation between the main shower observables and the nature of the primaries and predict that for the electromagnetic component, $N_{\rm max} \propto E$; $X_{\rm max} \propto \log E$ and $X_{\rm max} \propto \log A^{-1}$ with A the mass number of the primary nucleus; while for the muonic component, $N_\mu \propto A^{(1-\beta)} E^\beta$ with $\beta \simeq 0.85...0.95$. These important features of air showers constitute the basis for the identification of the primary particle with EAS (see next section). Similar features are also obtained in detailed Monte Carlo simulations of EAS development (Fig. 30.6), and have been observed experimentally.

Shower detection and cosmic-ray reconstruction. EAS have been detected with several techniques. Arrays of conventional particle detectors such as scintillators, water-Cherenkov stations or underground muon detectors, measure the lateral distribution of the shower front at ground, i.e., at a fixed depth. Due to the low cosmic-ray intensity especially at EeV energies (Figs. 30.1 and 30.7), the particle detectors are spread over large areas to compensate for the low flux, separated by distances that range from hundreds of meters to above 1 km. From the times at which the shower front hits several of these particle detectors, the arrival direction of the cosmic ray is measured with an accuracy typically better than $\sim 1^\circ$. Shower arrays measure a shower size parameter, proportional to the number of secondary particles, that can be related to the energy E of the primary particle. With several types of detectors working together, it becomes possible to effectively separate the electromagnetic and muonic components of the shower, thereby providing an estimate of the mass of the primary. The main arrays of particle detectors for EAS observation currently in operation are the surface detector of water-Cherenkov stations of the Pierre Auger Observatory in Argentina [125] spread over a total area of $\sim 3000\,{\rm km}^2$, and the Telescope Array (TA) of scintillators in USA ($\sim 700\,{\rm km}^2$) [126]. They typically work with almost 100% duty cycle and have measured many properties of the cosmic-ray flux (see next section).

Other arrays can measure the radiation emitted when the shower develops in the atmosphere, namely, optical Cherenkov radiation, fluorescence light, or radio emission in the MHz to GHz frequency range. Cherenkov detectors measure the forward-beamed incoherent emission at optical wavelengths. This can be achieved with arrays of individual elements such as at the Yakutsk [127] and Tunka-133 [128] observatories. A fluorescence telescope can monitor a large volume of the atmosphere and detect the isotropic fluorescence radiation emitted by the nitrogen molecules of air excited by the passage of the charged particles of the shower. The fluorescence radiation is produced in proportion to the energy dissipation and the shower size $N(X)$, allowing a reconstruction of the longitudinal profile of the energy deposit dE/dX of the shower as a function of atmospheric depth X and, in particular, providing a measurement of $X_{\rm max}$. With the fluorescence detection technique, the atmosphere is used as a calorimeter, with the integral $E_{\rm cal} = \int (dE/dX) dX$ called the calorimetric energy of the shower. An estimation of the primary energy with the fluorescence detection technique is obtained by adding to $E_{\rm cal}$ a correction to account for the invisible energy

introduced above. Fluorescence and optical Cherenkov detectors are limited by operation during clear and moonless nights which reduces their duty cycle to $\simeq 15\%$. The main fluorescence detectors currently in operation are those of the Pierre Auger Observatory [125] and TA [126].

Arrays of detectors of radio emission employ cost-effective elements (antennas) to detect the radiation in the 10's of MHz to GHz produced by the charged particles in the EAS. Radio emission is mainly due to two mechanisms: the transverse current induced by the magnetic field of the Earth that travels at the speed of light along shower axis, and the Askaryan effect i.e the radiation emitted by the excess of negative charge (e^-) that develops in the shower through Compton scattering of shower photons on e^- in the medium, as well as Möller and Bhabha scatterings. The measurement of the radiated energy in radio waves at ground also provides an estimate of the primary energy [129]. In a radio-quiet environment, these detectors can operate with a close to 100% duty cycle, only limited by thunderstorms and heavy rain. The principal arrays of radio antennas currently operating include the Auger Engineering Radio Array (AERA) and the ongoing deployment of the AugerPrime Radio Detector at the site of the Pierre Auger Observatory in Argentina [130], the Tunka-Rex [131] and Yakutsk [132] radio extensions in Russia, the LOw Frequency ARray (LOFAR) with its core detector in The Netherlands [133], and the Square Kilometer Array (SKA) in Australia [134].

Combining several types of detectors in the same array has proven very fruitful for increasing the accuracy in event reconstruction and energy calibration. Complementary measurements of the same event are expected to improve the determination of mass composition of the primary flux on an event-by-event basis. Projects under construction exploiting the simultaneous use of several detector kinds include, AugerPrime (water-Cherenkov stations, scintillators, underground muon detectors, fluorescence detectors and radio antennas) [135], TAx4 (scintillators and fluorescence detectors) [136], and the IceCube-Gen2 surface array (scintillators and radio antennas) [137]. Other arrays in the planning stages utilizing radio antennas are GRAND [138] and BEACON [139].

Experimental results. Cosmic rays in the PeV to EeV energy range have been regularly detected for decades, with energies up to $> 100\,\text{EeV}$. Despite the progress made in the field in the last 20 years, the nature and identity of their sources as well as the acceleration mechanisms that boost the particles to these extreme energies remain open questions. The understanding of CRs is mainly derived from analyzing their energy spectrum, several observables sensitive to their primary nature, and their arrival direction distribution. This is a challenging task mainly due to the small flux, with less than 1 particle per km^2 per year above 30 EeV (see Fig. 30.1), but also because the properties of CRs in this energy range can only be inferred indirectly from measurements of the EAS whose description relies on extrapolations of particle physics properties at energies several orders of magnitude above those achieved in terrestrial accelerators. Last but not least, since CRs are charged they are deflected by the galactic and intergalactic magnetic fields and their arrival directions at Earth point back only approximately to their actual sources.

Energy spectrum: The cosmic-ray spectrum observed at Earth (Fig. 30.1, with Fig. 30.7 highlighting the highest energies) can be characterized by a series of power-law functions proportional to $E^{-\gamma}$ with $\gamma \in (\simeq 2.5, \simeq 5.0)$ the spectral index that changes with energy. The production mechanism of CRs, mainly the unknown maximum CR energy achievable, CR composition and spectral index at the sources; the source type and distribution in the Universe; and the propagation through the Galaxy and the intergalactic space, all leave distinct imprints on the spectrum giving rise to several observable features. The differential flux over 5 orders of magnitude in energy is shown in Fig. 30.7. The flux has been multiplied by E^3 to highlight the deviations from a pure power law with a single value of γ. Several features are apparent, namely: a steepening at $\simeq 5\,\text{PeV}$ known as the *knee* (Fig. 30.1); another steepening around 100 PeV dubbed the *second knee*; the

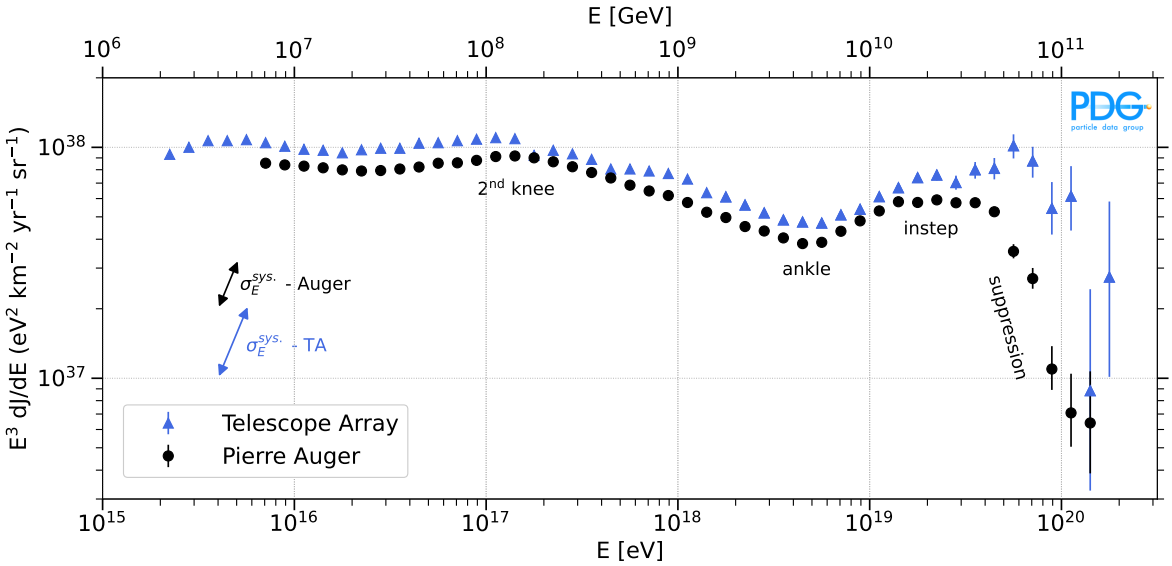

Figure 30.7: Measurements of the all-particle CR flux from Telescope Array (TA) [140] (blue triangles) and the Pierre Auger Observatory [33, 141] (black circles). The direction and magnitude of the systematic uncertainty on the flux due to the energy scale ($\sigma_E^{\rm sys}$) for TA and Auger is indicated by the corresponding arrows. For a comprehensive compilation of measurements see [142].

ankle, a flattening of the spectrum at around 5 EeV; a recently discovered feature corresponding to a further flattening starting at 10 EeV dubbed the *instep*; and the *suppression* of the spectrum starting around 50 EeV. These features are thought to be correlated with the observed changes on the average CR composition (see *Primary composition* below).

Cosmic-ray experiments have systematic differences in their energy scales and this manifests itself in differences in the measured spectrum, not only on the energy axis but also on the normalization when the flux is scaled with a power of the energy. The diagonal uncertainty bars in Fig. 30.7 serve to visualize the impact of these systematic differences on the spectrum. In the energy range above ~ 100 PeV the fluorescence technique is used to determine the primary cosmic-ray energy, with the atmosphere where the EAS develops functioning as a calorimeter. In the two state-of-the-art experiments for UHECRs, the Pierre Auger Observatory and the Telescope Array, a sub-sample of events is recorded simultaneously with the fluorescence (FD) and the surface detector (SD) arrays. With the SD, a shower size parameter is measured and calibrated against the energy measured with the FD. This approach provides a more direct method for determining cosmic-ray energy without relying on simulations. Differences in the energy scale between Auger and TA remain, however, primarily due to the use of different measurements of the amount fluorescence light emitted per unit of energy deposited, and to the different models for the invisible energy in EAS adopted. When these systematic uncertainties are accounted for, the spectra of the Pierre Auger Observatory and TA have been shown to agree within 5%, except in the energy region near the end of the instep feature and at the suppression.

Primary composition: The main observable sensitive to CR composition is the depth in the atmosphere along shower axis ($X_{\rm max}$) at which the number of particles in the shower is maximum. Observatories capable of detecting Cherenkov and/or fluorescence light induced by the passage of the EAS through the atmosphere, can measure $X_{\rm max}$ on an event-by-event basis. With sufficient statis-

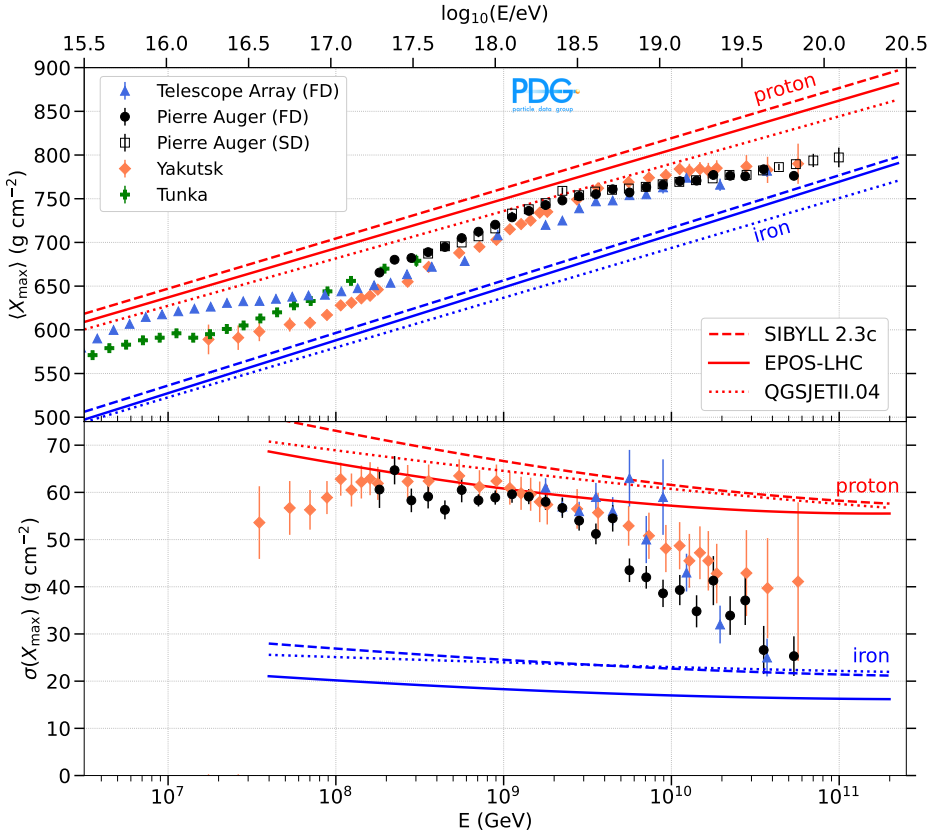

Figure 30.8: Measurements of $\langle X_{\rm max}\rangle$ (top) and $\sigma(X_{\rm max})$ (bottom) obtained by the Telescope Array [143, 144], Pierre Auger Observatory [145, 146], Yakutsk [127] and Tunka [147] UHECR detectors, compared to predictions for proton and iron nuclei using the hadronic models SIBYLL2.3c [148], EPOS-LHC [122] and QGSJET-II.04 [121]. Detection techniques: fluorescence (FD), Cherenkov (Yakutsk, Tunka, and TA below $\simeq 1$ EeV), and using the surface detector array of the Auger Observatory (SD). For a compilation including experiments using the radio technique see [142] and also [149].

tics, the distributions of $X_{\rm max}$ can be determined from which the average value $\langle X_{\rm max}\rangle$ and its fluctuations $\sigma(X_{\rm max})$ are obtained. A comparison with the $\langle X_{\rm max}\rangle$ and $\sigma(X_{\rm max})$ as predicted in simulations of EAS for different primaries and energies, as well as fits to the $X_{\rm max}$ distributions lead to the determination of the mean fractions of primary protons, helium, carbon-nitrogen-oxygen and iron in the cosmic-ray flux at Earth. However, the interpretation of any mass-sensitive observable relies on modeling hadronic interactions up to the highest energies where there are no data from terrestrial accelerators, and this introduces a considerable uncertainty in the determination of the mass. Also, due to intrinsic shower-to-shower fluctuations (see Fig. 30.6), an event-by-event determination of the mass of the primaries is not currently possible. Despite these limitations, the measurements presented in Fig. 30.8 alongside the predictions of EAS simulations for proton and iron primaries, reveal a broad trend toward a lighter composition at the knee, within the energy range of a few PeV. This is followed by a gradual rise in the average logarithm of the primary cosmic-ray mass, eventually leading to a heavier composition at around 100 PeV, although notable differences between experiments

exist. As the energy increases from 100 PeV up to ~ 2 EeV the measurements point consistently to a predominantly light composition with a large fraction of primary protons. Above that energy, the data from the largest statistical sample of events collected with the FD of the Pierre Auger Observatory indicate that the composition is mixed with the mean mass steadily growing. This observation is further supported by the shower-to-shower fluctuations of $X_{\rm max}$ also shown in Fig. 30.8. Though the data of the Telescope Array seem in apparent tension with this picture, they have been shown to be compatible with the results of the Pierre Auger and Yakutsk Observatories [150] within the current levels of statistics and understanding of systematic uncertainties. In particular, TA data are compatible with the mixed composition inferred by the Pierre Auger Collaboration [142].

The small duty cycle of the fluorescence technique combined with the steeply falling spectrum above $\simeq 50$ EeV prevents a statistically significant determination of the composition in this energy range. Information on the distribution of nuclear masses can be obtained with the surface arrays alone that work with a high duty cycle. Exploiting the arrival times of particles in the SD stations, that are known to contain information on the penetration of the shower in the atmosphere, measurements of $X_{\rm max}$ with the Pierre Auger Observatory were extended up to 100 EeV as shown in Fig. 30.8, after calibration of the mass-sensitivity of the SD with the measurements of $X_{\rm max}$ with FD at lower energy. Other novel methods such as those based on deep learning analysis techniques are also being explored [151]. Additionally, the arrays of radio detectors are also sensitive to $X_{\rm max}$ through the measurement of the shape of the radio emission footprint on the ground induced mainly by the electromagnetic component of the EAS. The radio technique demonstrates considerable potential in this respect and scalability, making it a cost-effective possibility for future UHECR detectors [149, 152].

Arrival directions: Anisotropies in the arrival direction of CRs are a key to discovering their sources. This is in principle feasible if the charges of the CRs and the galactic and extragalactic magnetic fields are well-enough determined. UHECRs are subject to the GZK effect, the energy loss of protons and heavier nuclei in interactions with the cosmic background. This imposes a horizon to possible sources of ~ 250 Mpc for protons and Fe nuclei, but shorter for nuclei in between these two, for instance ~ 5 Mpc for He and ~ 100 Mpc for Si at energies above $\simeq 50$ EeV [153]. Having only a limited range of source distances contributing to the signal makes it potentially feasible to identify sources or infer their properties statistically.

The Pierre Auger Collaboration has discovered a large-scale dipolar anisotropy at energies above 8 EeV with 6.9σ significance [154]. The amplitude of the dipolar anisotropy is $d = 0.073^{+0.010}_{-0.008}$ and the dipole points at a direction that is $\sim 115^\circ$ away from the Galactic Center, evidencing the extragalactic origin of UHECRs above this energy threshold. The dipole direction is not aligned with any obvious individual source, or with the expected CMB dipole, and is instead consistent with the local distribution of stellar mass (2MASS Redshift Survey), after accounting for the deflections expected in the Galactic magnetic field. A compelling feature is the growth of the amplitude of the dipole with energy in agreement with the expectation that particles of higher rigidity are less deflected by magnetic fields. Combining the Pierre Auger Observatory data set in the southern hemisphere and the smaller statistical sample of events from Telescope Array in the north, a full-sky coverage is achieved. The combined results regarding the dipolar anisotropy are compatible with the Pierre Auger Observatory-only results with no evidence of the existence of a quadrupole component. At energies between ~ 10 PeV and ~ 1 EeV the amplitude of the dipole is smaller (Fig. 30.5, bottom panel), but there is a trend for its direction to change from pointing close to the Galactic Center (GC) at low energy towards a direction away from the GC (Fig. 30.5, top panel) in the EeV energy range. This suggests that there is a transition between the galactic and extragalactic origin of UHECRs around the ankle in the spectrum, at a few EeV.

Hints of correlation of arrival direction of UHECRs with potential sources have been confirmed

in several analyses [142, 154, 155]. With data from the Pierre Auger Observatory a 4σ excess of events above 38 EeV was found in a region of angular radius $\simeq 27^\circ$ centered on the radio galaxy Centaurus A (CenA) [154]. The Telescope Array Collaboration has also reported an excess of events with energies above 57 EeV (the so-called *hot spot*) in the northern sky in the direction of R.A. = 144.0°, Dec. = 40.5°, with a 2.8σ significance and in an angular window of 25° [155]. Correlations with catalogs of potential UHECR sources have also been found. The sky viewed from the Pierre Auger Observatory is better modeled with a $\simeq 10\%$ flux excess in the directions of nearby starburst galaxies with a significance of 3.8σ and an energy threshold of 38 EeV with the correlation driven by the region of CenA where two prominent starburst galaxies are also located [154].

Despite the comprehensive observations made, it remains challenging to definitively ascertain the origin of UHECRs, primarily due to their deviation caused by the insufficiently constrained galactic and extragalactic magnetic fields. However, the constructed CR observatories designed to detect extensive air showers have the potential to also identify neutral particles of comparable energies. These include neutrinos, neutrons, and photons. Such searches can be made provided that methods are devised to separate photon and neutrino-induced EAS from those produced by the more abundant charged CRs, or in the case of neutrons if excesses in the sky are found. No photon or neutrino candidates have been clearly identified in the energy range around and above 100 PeV and upper limits to their flux have been obtained (see Fig. 30.13). UHECR observatories are thus also multi-messenger observatories of neutral particles [156]. These can be combined with gravitational wave detection and conventional radio, optical, X-ray and gamma-ray astronomy to greatly improve our knowledge about the most powerful objects in the Universe, as happened with the discovery of gravitational and electromagnetic radiation from the binary neutron star merger system in 2017 [157], with no neutrinos identified in temporal and spatial coincidence with it [158].

Astrophysical interpretation. A coherent picture of the nature and sources of CRs is emerging from the observations of the spectrum, composition and arrival directions, with many open questions. Cosmic rays below $\simeq 10$ PeV most likely have a galactic origin. The observed dipolar anisotropy in arrival directions imply that above 8 EeV they have their origin in extragalactic sources. One likely scenario is that the transition takes place at a few EeV, a hypothesis supported by the observed phase of the dipolar anisotropy changing around that energy from pointing to near the Galactic Center towards away from it (Fig. 30.5). Cosmic-ray rigidity Ze determines the maximum energy at which different particle species can be accelerated in the sources $E_{\rm max}(Z) = Z \times E_{\rm max}(Z = 1)$. As a consequence, protons would cutoff first in the spectrum, followed by helium, carbon ... up to iron. The observed increase with energy of the mass below the *second knee* could be interpreted as the signature of the end of the Galactic contribution dominating below the *second knee* [159]. As energy increases above a few times 100 PeV, the composition starts to become lighter. This could signify the emergence of an extragalactic component because no correlation with the densely populated Galactic plane is observed. A combined fit of the Pierre Auger Observatory measurements of the UHECR energy spectrum and composition [160] is compatible with the existence of this extragalactic component along with a second one at higher energy responsible for the sharp change in spectral index at the *ankle* feature in the spectrum at $\simeq 5$ EeV. Observations above the ankle suggest that each accelerated nuclear species from protons to iron, dominates in a narrow energy band of the UHECR spectrum produced through a combination of the individual composition peaks. In particular, the *instep* reflects the interplay between the flux contributions of the helium and carbon-nitrogen-oxygen components injected at the source with their distinct cutoff energies, all shaped by nuclear photodisintegration on background light during the propagation. This is consistent with the *suppression* above $\simeq 50$ EeV attributable to the $E_{\rm max}$

reachable at the cosmic accelerators along with the GZK and photodisintegration propagation effects. This comprehensive and unified understanding is continually evolving as additional data accumulates. Multi-messenger observations of the expected secondary neutrino and gamma-ray fluxes, or the lack thereof, will provide valuable constraints.

Hadronic interactions and Extensive Air Showers. EAS detectors probe energy and phase-space regions of hadronic interactions currently not accessible with terrestrial accelerators, although only in a very indirect manner. The tail of the distribution of $X_{\rm max}$ is sensitive to the attenuation length of primary p in the atmosphere, and the inelastic p-air cross-section can be inferred. In this manner, measurements of the p-air cross-section have been obtained at equivalent center-of-mass pp collision energy, $\sqrt{s_{pp}} > 40\,\text{TeV}$, and are in agreement with model predictions within systematic uncertainties [142]. The muonic component in the air shower is generally used as a probe of the hadronic interactions during the shower development. Various measurements of muons with energies in the $\simeq 100\,\text{MeV}$ to $\simeq 10\,\text{GeV}$ range produced in EAS, have revealed that hadronic models of multiparticle production fall short in predicting the observed number of muons above cosmic-ray energies of $\simeq 100\,\text{PeV}$ [161]. On the other hand, the simulated shower-to-shower fluctuations in the muon number that are particularly sensitive to the first hadronic interactions in the shower, are in good agreement with the measurements [162]. This indicates that the shortage in the number of simulated muons builds-up in multiple soft-QCD processes throughout the EAS development rather than being driven by only the first few and highest-energy interactions of the EAS. This constrains possible explanations of the so-called *Muon Puzzle* based on new physics beyond the Standard Model.

30.3 Gamma Rays

There is a well-studied flux of cosmic gamma rays (defined here as having energy greater than 1 MeV) present at the top of the atmosphere. Known as the diffuse gamma-ray flux, it has been measured with multiple space and ground-based instruments across a broad range of energy. On top of the diffuse one, many discrete sources have been found with either a steady gamma-ray flux or variability of many types.

30.3.1 *Observational Instruments: Space borne and Ground based*

Space borne γ-ray detectors, including AGILE [163], DAMPE [164], CALET [165], mainly Fermi-LAT [166], cover the energy range above 10 MeV up to 100 GeV. With the wide Field-of-View (FoV), they effectively survey the whole sky for steady γ-ray sources, and monitor all types of transient phenomena such as flares of Active Galactic Nuclei (AGN) and γ-ray bursts (GRBs). Above 100 GeV, ground-based Imaging Air Cherenkov telescope (IACT) experiments H.E.S.S [167], MAGIC [168], VERITAS [169] and CTA-LST [170] are very effective observational instruments. Using the stereo measurement technique, the IACT arrays achieve the angular resolution of the arrival direction of γ-rays at the level of 3 arc minute which is necessary for the high precision measurements of discrete sources. The small Field-of-View (FoV) of the telescopes and low-operation duty cycle make the all-sky surveys for new sources difficult. Only H.E.S.S scanned the region along the Galactic plane around the Galactic Center [171], as shown in Figure 30.9. Non-imaging Cherenkov light technique is also developed trying to cover wider FoV, e.g. in the TAIGA experiment [172]. The most suitable detectors for all-sky surveys are extensive air shower detector arrays at high altitudes, such as ARGO-YBJ [173], AS$_\gamma$ [174], HAWC [175] and LHAASO [176]. They are operated with very high duty cycle, typically $> 95\%$, have compatible sensitivity for discrete sources to IACT telescopes in much wider FoV in the same energy band, and higher sensitivity at higher energies above 10 TeV. In Table 30.1, the main features of the major facilities in γ-ray astronomy are listed.

Instrument	**energy range**	**Effective area** (m^2)	**sensitivity** (milli-CU†)	**energy resolution** (%)	**PSF** (°)	**FoV** (sr)	**duty cycle** (%)
Fermi-LAT[a)]	20 MeV - 300 GeV	~ 0.95	10 - 30	8 - 18	0.15 - 3.5	~ 2.4	~ 60
H.E.S.S.[b)]	10 GeV - 50 TeV	$\sim 10^5$	~ 5	15	< 0.1	~ 0.03	$\sim$10
MAGIC[c)]	$\geq$ 30 GeV	$\sim 10^5$	~ 7	16	≤ 0.07	0.02	$\sim$18
VERITAS[d)]	50 GeV - 50 TeV	$\sim 10^5$	~ 5	10 - 15	0.08 - 0.13	0.02	10-14
CTA-LST1[e)]	20 GeV - 300 GeV	$\sim 10^4$	~ 10	10 - 30	0.05 - 0.1	0.02	$\sim$10
ASγ[f)]	10 TeV - 1 PeV	$\sim 7 \times 10^4$	~ 200	20 - 40	~ 0.8	~ 2.0	90
ARGO-YBJ[g)]	50 GeV - 10 TeV	$\sim 0.8 \times 10^4$	~ 300	>13	~ 0.5	~ 2.0	86
HAWC[h)]	100 GeV - 100 TeV	$\sim 3 \times 10^4$	~ 50	20 - 50	~ 0.69	> 1.5	95
LHAASO-WCDA[i)]	100 GeV - 20 TeV	$\sim 0.8 \times 10^5$	~ 12	$\sim$33	0.2 - 0.84	~ 2.0	95
LHAASO-KM2A[i)]	10 TeV - 4 PeV	$\sim 10^6$	~ 12	15 - 40	0.2 - 0.6	~ 2.0	95

Table 30.1: Facilities for γ-ray detection and their specifications in reference *a*) [166], *b*) [177], *c*) [178], *d*) [179], *e*) [170], *f*) [174], *g*) [173], *h*) [175], *i*) [176]. † milli-CU = 10^{-3} Crab Unit.

30.3.2 *Diffuse Gamma Rays*

The majority of photons detected at high energies are characterized as diffuse emission that is not resolved as discrete sources. The observations of the diffuse emission are mainly carried out by wide FoV detectors, including space missions, OSO-3 [180], SAS-2 [181], COS-B [182], CGRO/EGRET [183], and Fermi-LAT [184] at energies below 1 TeV, and ground-based experiments Milagro [185], H.E.S.S [171], ARGO-YBJ [186], ASγ [187] and LHAASO [37] at energies up to 1 PeV. Evident in Figure 30.9, the dominant component comes from the plane of the Galaxy (i.e., $|b| \lesssim 10°$, and is referred as the Galactic Diffuse Emission (GDE). Precise measurement of the GDE flux strongly depends on the subtraction of the contamination from discrete sources most of which are found spatially extended. With significantly improved sensitivity of source detection, Fermi-LAT and LHAASO largely reduce the contamination by removing the regions associated with known sources. In case of LHAASO, the flux in the Galactic plane with longitudes of $15° < l < 235°$ and latitudes of $|b| < 5°$ is well measured [37].

Three components are expected in GDE, namely γ-rays from the decay of neutral pions produced via inelastic collisions between energetic cosmic ray nuclei and the interstellar medium (ISM); bremsstrahlung radiation of electrons and positrons in ISM; and inverse Compton scattering of electrons and positrons off the interstellar radiation field. Possible annihilation or decay of dark matter (DM) particles might also give rise to diffuse γ-rays particularly in the densest region of the Galaxy. Therefore, GDE serves not only as a very important tool to probe the production, propagation, and interaction of cosmic rays, but also as a route to search for DM in any excess over the expectation, which is based on assumptions of the cosmic-ray spatial distribution, composition, energy spectrum and on the ISM column density along the line-of-sight. The search for DM also depends on the fraction of the contribution by the unresolved dim discrete sources in the GDE. Unfortunately, all of the assumptions have their own large uncertainties at present.

Evidence of an isotropic component of diffuse γ-ray emission, presumably of extragalactically originated, was obtained with the measurement of its spectrum by CGRO/EGRET [188] and Fermi-LAT [189]. The Fermi-LAT spectrum covers the energy range from 0.1 GeV to 820 GeV and is well described by a power-law with an exponential cutoff. It is consistent with a scenario of a discrete source population, such as blazars with power-law spectral shape, dominating the emission and experiencing attenuation due to the extragalactic background light (EBL) [189]. Contributions from the cascade of very-high-energy gamma rays and UHECRs are not ruled out as a fraction of

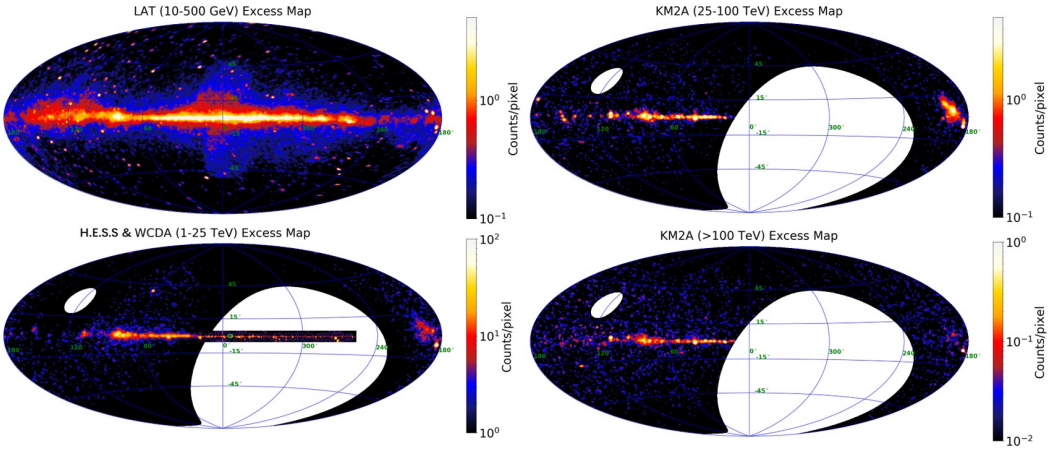

Figure 30.9: The GeV γ-ray sky maps surveyed by Fermi-LAT [184], LHAASO [3] and H.E.S.S [171] from 1 GeV to 100 TeV and above.

the extragalactic diffuse emission.

30.3.3 *Discrete Gamma Ray Sources*

As a neutral component of cosmic rays, γ-rays directly reach the earth from their sources, thus allowing us to identify the origin of the photons by association with known celestial objects or events. As shown in Figure 30.9, the source-associated contributions are revealed directly by the bright spots whose sizes are due to the point-spread-function (PSF) of the instruments and the intrinsic spatial extensions of the sources. It is also clearly shown that the sources are divided into two groups: *Galactic* and *extragalactic*.

Galactic Sources More than 6600 sources have been found emitting γ-rays in the Milky Way. Most of them have steady photon emissions over a wide energy range above 0.1 GeV up to 2 PeV. 43 of them have emission of γ-rays above 0.1 PeV referred as *PeVatrons* since the parent particles that emitted the photons must be accelerated above 1 PeV on average in the source regions. Variability of the photon fluxes has also been observed from known objects such as pulsars and binary systems or transient phenomena.

A. Sources with steady emissions are the majority of Galactic γ-ray emitters which are well documented in reviews [190], [191], [192] and in γ-ray source catalogs [193] (for $<$ 100 MeV), 4FGL (for 0.1-300 GeV) by Fermi-LAT [194], TeV-Catalog available on-line (http://tevcat.uchicago.edu) and the newly released 1LHAASO (for 1-2000 TeV) by LHAASO [3]. All associations with known celestial objects, such as SNRs, PWNe, young massive-star clusters (YMC) are discussed in the corresponding catalog papers (e.g. individual catalogs collected in http://tevcat.uchicago.edu). Most of the sources, particularly for their high-energy emission above tens of TeV, remain unidentified. Among the identified ones, the Crab [195] and RX J1713-3946 [196] are the most extensively studied objects and constitute paradigmatic examples of PWNe and SNRs.

The Crab has a compact PWN powered by the rotation energy of the pulsar in its heart. Electrons and positrons in the wind are accelerated at the termination shocks and emit γ-rays through synchrotron radiation at energies lower than 0.1 GeV. Simultaneously, accelerated electrons and positrons boost soft background photons, such as those in the cosmic microwave background, to energies well above 1 GeV via inverse Compton scattering. Figure 30.10 shows the spectral energy density (SED) of the Crab nebula with a fit using a simple one-zone leptonic model. It

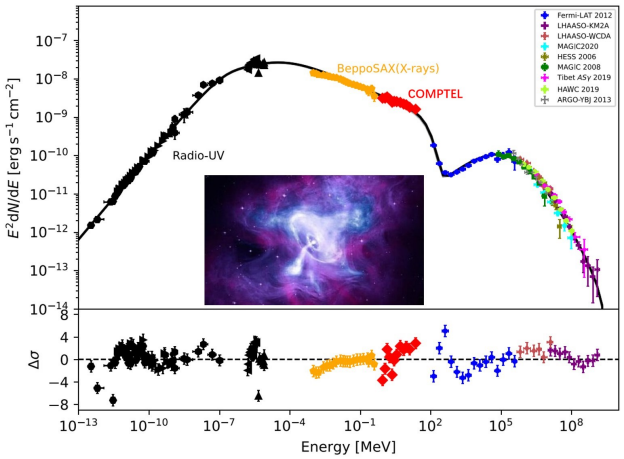

Figure 30.10: Spectral energy density (SED) of photons from the Crab from sub-μeV to 1.1 PeV. Above 1 TeV, data are collected from 7 experiments listed in legend in the upper panel. The lower panel shows the deviation between data and the model based on a widely accepted one-zone leptonic origin in the nebula. Only Fermi-LAT and LHAASO data are shown for simplicity. Inset is the X-ray image of the nebula by Chandra [197].

generally describes the radiation of the nebula over energies up to $E_\gamma \sim 1.1$ PeV, implying that electrons and positrons are confined in a small region of $\simeq 0.2\,$pc by a magnetic field of intensity $B \simeq 110\,\mu$G and are accelerated to energies as high as $\simeq 2.3\,$PeV. This requires a surprisingly high acceleration rate, $\eta = \bar{\epsilon}/B = 0.14(B/100\mu\text{G})(E_\gamma/1\text{ PeV})^{1.54}$ PeV, at the level of 15%, where $\bar{\epsilon}$ is projection of the electric field averaged over the particle trajectory. This rate is 3 orders of magnitude higher than that in the normal shock environment such as in SNRs, revealing the existence of a so-called 'extreme accelerator' in the middle of the nebula [195]. The flux of photons above 0.8 PeV indicates some deviation from the pure leptonic scenario implying that a hadronic component might be responsible. It could be a hint of the super PeVatron which may contribute to the Galactic cosmic rays above the knee [195] (see Fig. 30.1).

RX J1713.7-3946 is one of the brightest objects in the TeV sky, and is the first SNR shell to be confirmed as a TeV gamma-ray source [196]. The detailed TeV morphology reveals a shell structure similar to the X-ray observations, indicating that particles are accelerated to very high energy therein. The TeV gamma-ray spectrum extends to nearly 100 TeV. It is not determined yet whether the gamma-rays are produced via Inverse Compton scattering of relativistic electrons (leptonic process), or via neutral pion decay with the pions produced in the inelastic scattering of CR protons with ambient gas (hadronic process) [198]. Nevertheless, the spectral information demonstrates the efficient acceleration of charged particles to energies beyond 100 TeV in this object. The latest H.E.S.S observations also found that the TeV gamma-ray emission region extends significantly beyond the X-ray emitting shell [199], which may be due to either the escape of particles from the shell or to particle acceleration in the shock precursor region.

B. Variable sources Crab flares, binaries and pulsars are observed in the Galactic γ-ray sky. Their activity varies on timescales from a fraction of one second (pulsars), to days (Crab Nebula, Novae), weeks, months or even years (γ-ray binaries). Various analysis pipelines are developed mainly by the LAT collaboration to search for and monitor γ-ray transients.

The Crab Nebula shows flare activities on a timescale of days [200]. The instability is observed only in GeV band by AGILE and Fermi/LAT. The flaring mechanism is still unclear with a couple

of models being under debate.

Each γ-ray binary is composed of a compact object (pulsar or black hole) and a massive star. Their γ-ray emissions characterized by the orbital modulation, with time scales ranging from 3.9 days (LS 5039) to $\sim$ 47 years (PSR J2032+4127). Microquasars are also binary systems that launch powerful jets from the compact objects by accreting matter from their companions. Three microquasars have been detected namely, Cyg X-1, Cyg X-3, and SS 433. They have shown γ-ray activities correlated with orbital motion [201], jet precession [202], X-ray state changes [203], and flares [204]. Eta Carinae is the only colliding wind binary firmly detected, showing orbital modulation in the γ-ray emission in a period of 5.54 years [205].

Pulsars show steady pulsation on their spin periods ranging from several milliseconds to seconds in GeV band [206], thereby qualifying as γ-ray pulsars. Only the Crab and Vela pulsar are pulsating in TeV [207] [208]. PSR J2021+4026 is observed for the γ-ray flux variability on time scales of several years [209], making it the only variable γ-ray pulsar. Many millisecond pulsars themselves are γ-ray pulsars showing periodic variability in milliseconds [210]. γ-ray eclipses and orbital modulations have been detected in several binaries hosting millisecond pulsars, usually on the time scale of hours to days, arising from the intra binary shock between the pulsar wind and stellar wind [211] [212]. Millisecond pulsars could transit between spin-down-powered state and accretion-powered state. Variability in the γ-ray flux is observed accompanying these changes [213].

Novae outbursts have been detected in γ-rays, arising from the particle acceleration at shocks and last for months [214]. RS Ophiuchi is the first nova with its outburst detected in TeV up to 1 month [215].

Extragalactic Sources The majority of extragalactic γ-ray sources are active galactic nuclei (AGN). The fourth catalog of AGNs (4LAC) by LAT for 8 year observations contains 2863 objects located at high Galactic latitudes ($|b| > 10^\circ$) while 344 others were found at lower latitudes [216]. 98% of them are blazars. The blazar population consists of Flat Spectrum Radio Quasars (FSRQs), BL Lac-type objects and unknown types [216]. The Data Release 3 adds 587 more blazars and 4 radio galaxies to the catalog [217]. More than 70 blazars and a few radio galaxies are detected in the very high-energy (VHE) band, namely photon energy greater than 0.1 TeV, by imaging atmospheric Cherenkov telescopes (IACT) (http://tevcat.uchicago.edu).

Blazars belong to a class of AGN where the jets are oriented at a relatively small angle with respect to the line of sight. This specific viewing angle allows us to observe the emission from those jets with significant Doppler boosting. The photon flux in the jets may enhance significantly with respect to that in quiet states, a phenomenon referred to as blazar flares. They are simultaneously observed over a wide energy band from radio to VHE γ-rays with timescales ranging from a few minutes to year [218] [219]. The broad-band SED of blazars typically shows two humps of non-thermal radiation. The one in the lower energy range from radio to X-rays is generally attributed to synchrotron emission from relativistic electrons and positrons in the jet, while the origin of the hump at higher energies is still under debate. Possible emission mechanisms are the IC scattering of accelerated leptons off low energy photons, which are inside jets or from outside regions [220], or decay of neutral pions produced in collisions of accelerated protons against ambient matter [221], or some combination of the two processes.

The ground-based EAS experiments are suitable γ-ray detectors for monitoring the flares of AGNs with the advantages of large FoV and full duty cycle of operation. The ARGO-YBJ collaboration reported a long-term continuous monitoring of Mrk 421 and Mrk 501 [222–224], the two brightest blazars in the TeV sky. The γ-ray flux shows a good long-term correlation with that in the X-ray band. HAWC detected the persistent emission from those two AGNs [225]. Recently, the

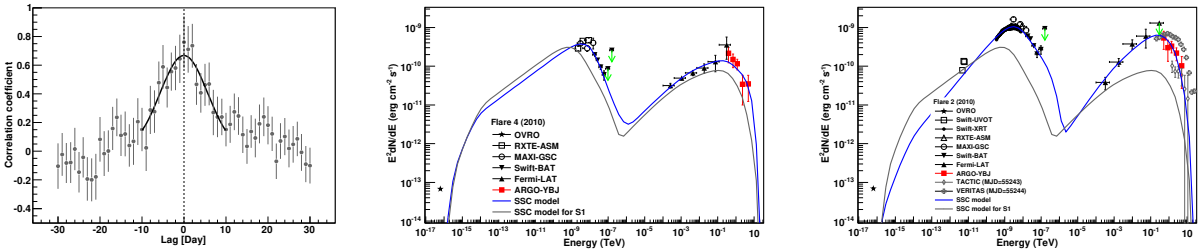

Figure 30.11: The multi wavelength analysis of Mrk 421 involving measurements over wide energy range from radio to TeV γ-ray during 4.5 years when ARGO-YBJ and LAT were operated [224]. The discrete correlation function between the light curves in X-ray band and TeV γ-ray band is calculated and clearly shows no time lag between emissions in the two bands [224] (left panel). The SED significantly changes from steady states (grey solid lines in middle and right panels) to flaring states depending on the strength of flares. Comparing a small flare in the middle panel and a larger one in right panel, the later has harder SED in VHE band [222].

LHAASO collaboration reported eight sources detected at Galactic latitude $|b| > 12°$, among which some are AGNs, including well-known emitters, such as the radio galaxy M87, VER J0521+211 and 1ES 1215+303 [3].

Using data for 4.5 years when ARGO-YBJ and Fermi-LAT simultaneously operated from 2008 to 2013, the ARGO-YBJ collaboration realized the long-term multi wavelength observation of Mrk 421 in all bands of radio, optical, X-ray, GeV, and TeV gamma-rays [224]. The well-known correlation [226] between the photon fluxs in X-ray band and TeV γ-ray band is investigated in a quantitative way, namely the discrete correlation function between the light curves in two energy bands being calculated. No time lag in the scale of days is found(see Figure 30.11). This is regarded as evidence of favoring the one-zone Self-Synchrotron Compton scattering scenario [222].

Flares happened in that time window are systematically analyzed and clear correlation between the strength of flares and features of the SEDs are observed as an example shown in Figure 30.11. Detailed investigation of SEDs implies that various particle acceleration mechanisms, such as relativistic diffusive shock acceleration, might be responsible for different flares. A similar analysis is carried out with data during outbursts of Mrk 501. The SEDs in the VHE band are observed to be harder during flares than that in the quite period. The detection of energetic photons above 10 TeV and the hardness of the SED hint some exceeds over the expectation of one-zone SSC model [223].

Gamma-Ray Bursts (GRBs)

GRBs are violent explosions observed in distant galaxies, characterized by a rapid flash of γ-rays lasting from a fraction of a second up to several hundreds of seconds. The emission from GRBs occurs in two stages, namely the prompt emission phase and the afterglow phase, as can be seen in Figure 30.12.

In the second catalog of Fermi/LAT-detected GRBs, covering the first 10 yr of operations, 169 GRBs are detected above 100 MeV [231]. The high-energy emission generally lasts much longer than the prompt keV-MeV emission. The widely discussed scenario for the extended GeV emission is synchrotron radiation by relativistic electrons that are accelerated in shocks resulting from the interaction of the jet with the surrounding medium [232, 233].

VHE emission has been detected from just a few GRBs by IACTs during the afterglow decay phase. MAGIC slewed to the direction of GRB 190114C only $\simeq$ 60 seconds after the trigger

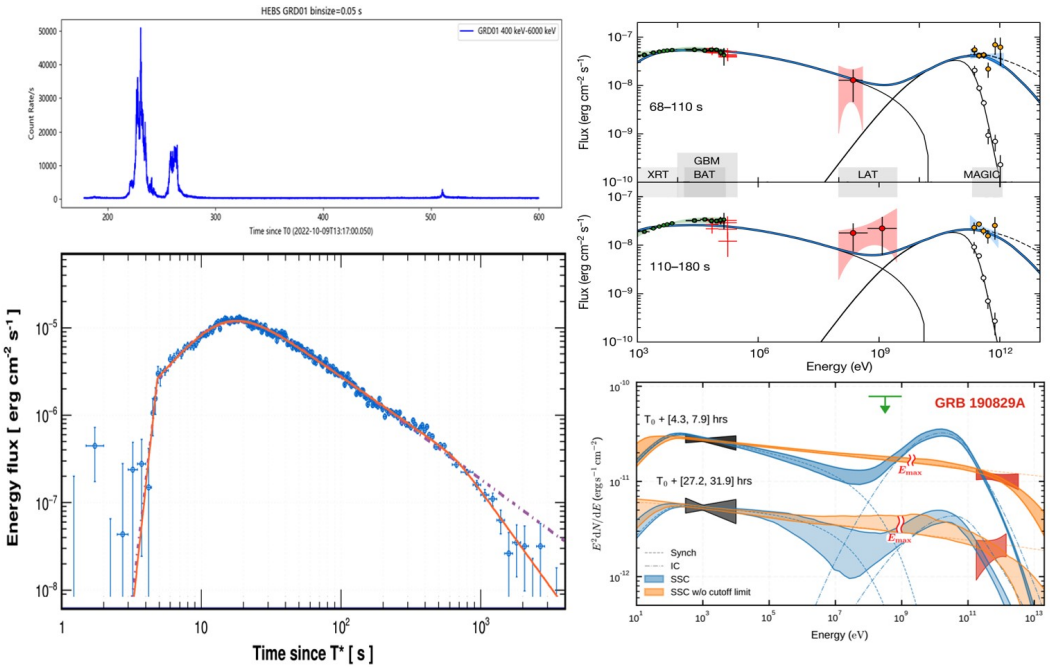

Figure 30.12: The typical multi-wavelength measurement of the light curves of the γ-ray burst GRB 221009A in the GeV band [227] (top left) and in the TeV band [228] (bottom left). The clear different structures of the brightness variation patterns indicate the different origins of the synchrotron radiation and inverse Compton scattering of leptons accelerated by the internal and external shock waves, respectively. The spectral energy distributions of the GRB 190114C and GRB 1908129A, respectively measured by MAGIC [229] (top right) and H.E.S.S [230] (bottom right). The Self-Synchrotron Compton scattering model of the afterglow is marginally supported in the observations covering a wide energy band from X-rays to TeV γ-rays.

and detected photons above 300 GeV from the burst for the first 20 minutes [234]. This VHE emission is explained by inverse Compton up-scattering of synchrotron photons by high energy electrons in the external shock [229], as shown in the right-upper panel of Figure 30.12. Two other events, GRB 180720B and GRB 190829A, were also detected during the afterglow decay phase by H.E.S.S [230, 235], the unexpected SED is shown in the right-lower panel of Figure 30.12.

The brightest-of-all-time GRB 221009A serendipitously occurred within the FoV of LHAASO. More than 64,000 photons (above 0.2 TeV) were detected within the first 3000 seconds by LHAASO-WCDA [228]. The detection covers both the prompt emission phase and the early afterglow in the TeV band, revealing the onset of afterglow emission in the TeV band for the first time, as shown in the left panels of Figure 30.12. In addition, the unprecedented photon statistics of the TeV emission enabled identifying a jet break in the light curve, indicating an opening angle of GRB 221009A of $\sim 0.8°$. This is consistent with the brightest core of a structured jet, explaining the unexpected high isotropic equivalent energy of this GRB. LHAASO-KM2A registered more than 140 photons with energies above 3 TeV from GRB 221009A (to be published). The intrinsic energy spectrum of gamma-rays is well fitted by a power law after correcting for EBL absorption, with the highest energy photon above 13 TeV traveling over a distance with red shift $z \sim 0.152$(TBP).

Tests on Lorentz Invariance Violation (LIV) Tests on LIV are feasible and thus, limits can be set using the highest energetic photons collected from remote sources. Any tiny violation of the invariance leads the fundamental dissipation relation to be rewritten [236] as $E^2 = m^2c^4 + p^2c^2(1 + A_1 pc/M_p c^2 + A_2(pc/M_p c^2)^2 + ...)$, where E, p are the energy and momentum of a particle with the mass m, the M_p is the Plank scale and A_1, A_2 are theoretic parameters of the violation at the first and second order levels. This must lead instability of photons that may decay on their way to the Earth [237]. The first order violation effect due to the decay channel $\gamma \to e^+ + e^-$ has not been found at energies ∼5 orders of magnitudes higher than the Planck scale, regarded as the null evidence of the quantum gravitational effect. However, the limit due to second-order effect caused by decay channel $\gamma \to 3\gamma$ is still found still ∼3 orders of magnitudes below the Planck scale, using the latest observations of photons up to 1.4 PeV from the Cygnus X direction [238].

30.4 Neutrinos

In contrast to charged particles, neutrinos are not deflected by electromagnetic fields and thus point back to their origin, making them appealing messengers for astronomical observations. In addition, neutrinos of cosmic origin, or produced in the atmosphere of the Earth, allow us to study particle physics in a kinematic regime not accessible to date to accelerator experiments. In the following, we will consider neutrinos with energies at the GeV energy scale and above.

30.4.1 *Production of high-energy neutrinos*

High-energy neutrinos can be produced in hadronic interactions in a variety of astrophysical objects (*astrophysical* or *cosmic* neutrinos), in scattering of extremely energetic protons (p) with the cosmic microwave background (*cosmogenic* neutrinos) and by cosmic-ray interactions in the Earth's atmosphere (*atmospheric* neutrinos). The main production chain is (A denoting atomic nuclei and X a hadronic system)

$$p(A) + p(A,\gamma) \to \pi^{\pm} + X \quad \text{with subsequent decays} \quad \pi \to \mu\,\nu_\mu \text{ and } \mu \to e\,\nu_\mu\,\nu_e\,, \tag{30.1}$$

resulting in a ratio $\nu_e : \nu_\mu : \nu_\tau = 1 : 2 : 0$ (not distinguishing here between ν and $\overline{\nu}$). If the source density is high, muons can lose most of their energy before decaying, yielding a ratio $0 : 1 : 0$ in the extreme case. If protons were kept in the source region by magnetic fields without interacting, and only neutrons could escape and then decay via $n \to p + e^- + \overline{\nu}_e$, the ratio would be $1 : 0 : 0$. Over cosmic distances, flavor mixing turns these ratios to 0.30:0.36:0.34 for the first source scenario (1:2:0), 0.17:0.45:0.37 for the second (0:1:0) and 0.55:0.17:0.28 for the third scenario (1:0:0) [239].

30.4.2 *Measurement methods*

Most experiments targeting high-energy cosmic neutrinos are based on the detection of Cherenkov light induced by charged secondary particles produced in neutrino interactions. This includes underground detectors like Super-Kamiokande with its fiducial volume of $22.5 \times 10^3\,\mathrm{m}^3$ (see Sect. 36.3.1) and underwater/ice detectors like ANTARES, KM3NeT or IceCube, the latter with a volume of $10^9\,\mathrm{m}^3$ (see Sect. 36.3.2). Neutrinos with energies exceeding some tens of PeV can be also detected via the coherent emission of Cherenkov radiation at radio wavelengths in ice or other radio-transparent media (e.g. ANITA or RNO-G, see Sect. 36.3.3). Neutrinos with EeV energies could be identified via extensive air showers starting too deep in the atmosphere to be due to particles with strong or electromagnetic interaction. Alternatively, they could be detected via slightly upward-directed air showers from the decay of tau leptons generated in interactions of Earth-skimming or mountain-traversing ν_τ [240]. These signatures could be observed by cosmic-ray experiments such as the Pierre Auger Observatory [241].

30.4.3 *Diffuse fluxes*

Atmospheric neutrinos The flux of atmospheric neutrinos as measured by different experiments is shown in Fig. 30.13. The production chain for *conventional* atmospheric neutrinos follows eq. (30.1), with an observed ratio $\nu_e : \nu_\mu = 1 : 2$ at energies of a few GeV (where almost all muons decay in the atmosphere), and a ratio below $1 : 10$ at TeV energies, where muons reach the ground before decaying. The flux of muon neutrinos with energies below 100 GeV from the lower hemisphere is reduced due to neutrino oscillations, reducing the $\nu_e : \nu_\mu$ ratio at the lowest energies. The flux of ν_e is obtained by subtracting the number of neutral-current muon neutrino interactions (as deduced from the measured charged-current muon neutrino reactions) from the number of contained events without a muon track and converting the resulting E_{ν_e} distribution into the ν_e flux using the differential cross sections for CC and NC ν_e-nucleon scattering. The conventional atmospheric neutrino flux dominates in the GeV to TeV region, following an $E_\nu^{-3.7}$ power law.

Prompt atmospheric neutrinos are produced by the decay of hadrons containing a charm or bottom quark, the production of which is strongly suppressed. Since they are produced early in the air shower and decay before losing energy, however, the energy spectrum of prompt neutrinos is expected to be harder ($E_\nu^{-2.7}$) and to dominate the atmospheric neutrino flux at its highest energies. The corresponding theoretical prediction has large uncertainties related to the cosmic-ray spectrum and mass composition, the model for heavy-flavor production, and the parton distribution functions [242]. At present, experimental measurements only provide upper limits for the prompt flux (see e.g. Fig. 30.14 where the prompt component was fitted to zero).

Diffuse extragalactic neutrino flux In 2013, a diffuse and isotropic flux of neutrinos of astrophysical origin was discovered with the IceCube Neutrino Observatory. The flux was identified with the so-called HESE (high-energy starting events) selection as an excess of neutrino events at high energies over atmospheric neutrinos and a background of misreconstructed atmospheric muons (see Fig. 30.14, for the 7.5-year HESE sample [251]). Similar high-energy excesses were also identified for tracks entering the detector from outside [252], and for fully contained cascade events. Evidence for this flux has meanwhile also been reported by ANTARES [253] and Baikal-GVD [254], albeit with much lower significance. The measured fluxes are consistent with a parameterization as power-law functions proportional to $E_\nu^{-\gamma}$, with the normalization factor and the spectral index γ as parameters. The resulting γ values vary from 2.2 to 2.5 for different event classes covering different energy ranges.

Different production mechanisms result in different neutrino flavor compositions at sources and, after neutrino oscillations over astrophysical distances, at the Earth. An IceCube study of the event topologies [239] slightly favors $\nu_e : \nu_\mu : \nu_\tau = 1 : 2 : 0$ at the source (pion decay according to eq. (30.1) versus $0 : 1 : 0$ (damped muons) and disfavors a $1 : 0 : 0$ scenario (neutron decay).

A single event with energy 6.05 ± 0.72 PeV has been detected in IceCube [247]. It is compatible with having been generated by the resonant process $\bar{\nu}_e + e^- \to W^- \to$ hadrons at $E_\nu = 6.3$ PeV (Glashow resonance) [255]. A statistically significant observation of the Glashow resonance would reveal the presence of electron antineutrinos in the astrophysical flux and could provide information about their production process: the expected ratio $\bar{\nu}_e : \nu_e$ depends on the mass composition of cosmic-rays and also on the photon density and the magnetic field strength of the source [256].

Cosmogenic neutrinos Cosmogenic neutrinos stem from the decay of charged pions generated in interactions of ultra-high-energy cosmic rays with cosmic microwave (a) and infrared (b) background radiation ($p + \gamma \to n + \pi^+$) [257] and from the decays of neutrons produced in photodisintegration processes [258, 259] (c). The neutrino flux at EeV energies is expected to be dominated by (a) and

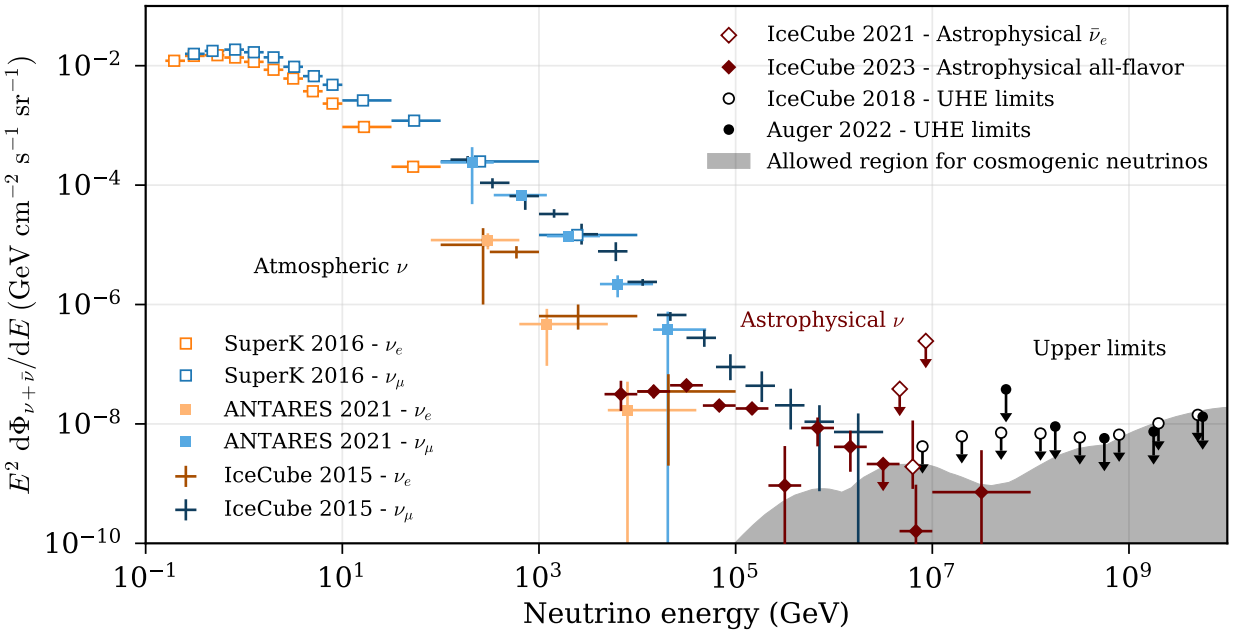

Figure 30.13: Measured energy spectra of atmospheric and cosmic diffuse neutrino fluxes. Experimental limits at highest energy are compared to model predictions for cosmogenic neutrinos [160]. All fluxes are normalized to one flavor ($\nu+\overline{\nu}$), assuming a ratio $\overline{\nu}:\nu=1$ and, for cosmic neutrinos, a ratio $\nu_e:\nu_\mu:\nu_\tau=1:1:1$ at Earth. Data sources: SuperK 2016 [243]; ANTARES 2021 [244]; IceCube 2015 ν_e [245]; IceCube 2015 ν_μ [246]; IceCube 2021 astrophysical $\bar{\nu}_e$ ($\nu+\overline{\nu}$ flux derived from a single candidate event for the Glashow resonance) [247]; IceCube 2023 astrophysical all flavor [39]. The limits at the highest energies are taken from [248] (IceCube) and [249] (Auger). They are shown in the energy bins used for the corresponding analyses and have been adjusted to bin widths of one decade. The region allowed for the expected cosmogenic neutrino fluxes is taken from [250] (see also Fig. 36.10).

(c).

Measurement methods and experimental data are described in Sect. 36.3.3. and Fig. 36.10. The expected flux can be estimated from the measured spectrum and composition of charged cosmic rays, using the CMB density and the well measured properties of proton and nuclear interactions with photons at a center-of-mass energy in the GeV range. The current uncertainty of these predictions exceeds one order of magnitude. Figure 30.13 reproduces the presently tightest limits and compares them to the region for which cosmogenic neutrino fluxes would be consistent with those limits (as of 2019) and cosmic-ray analyses [250].

Neutrinos from the Galactic Plane The Milky Way is an emitter across the electromagnetic spectrum ranging from radio to gamma-rays. A large part of the observed gamma-ray flux is believed to consist of photons from the decays of π^0s produced by cosmic rays colliding with the interstellar medium. The TeV diffuse neutrino flux from the corresponding $\pi^\pm$ decays along the Galactic plane has been estimated with different models, ranging from a simple extrapolation of Fermi-LAT gamma-ray data to higher energies, to more sophisticated approaches (see e.g. [260]).

First hints for a TeV neutrino emission from the Galactic Ridge have been reported by the

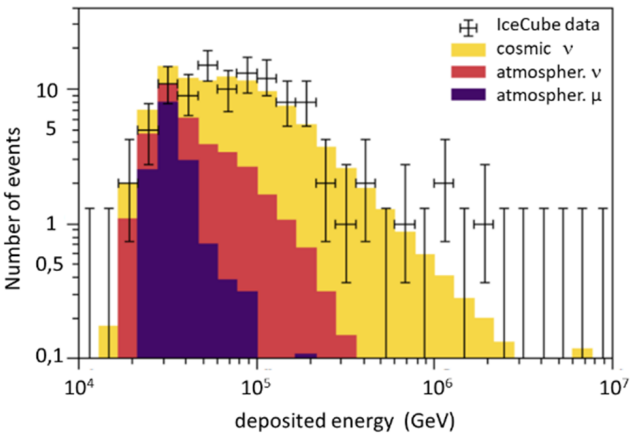

Figure 30.14: Measured (data points) and expected (histograms) distributions of the deposited energy measured in the IceCube detector for events passing the HESE selection, which strongly suppresses down-going atmospheric neutrinos by vetoing accompanying muons. The cosmic neutrino flux has been assumed to follow an unbroken power law in E_ν. Its normalization and spectral index, as well as the normalizations of the conventional and prompt atmospheric neutrino and the atmospheric muon contributions were fitted to the data, where only the region above 60 TeV was used to constrain the cosmic neutrino flux.

ANTARES collaboration [261]. IceCube has measured the flux of galactic neutrinos with a significance of 4.5σ against the only-background-hypothesis [262]. Figure 30.15 shows a map of the Galactic plane with the point-by-point pre-trial significance of the IceCube neutrino observations. While the overall signal is consistent with the modeled diffuse emission from the Galactic plane, a significant part could also arise from a population of unresolved point sources. All individual "warm spots", however, are statistically consistent with background fluctuations.

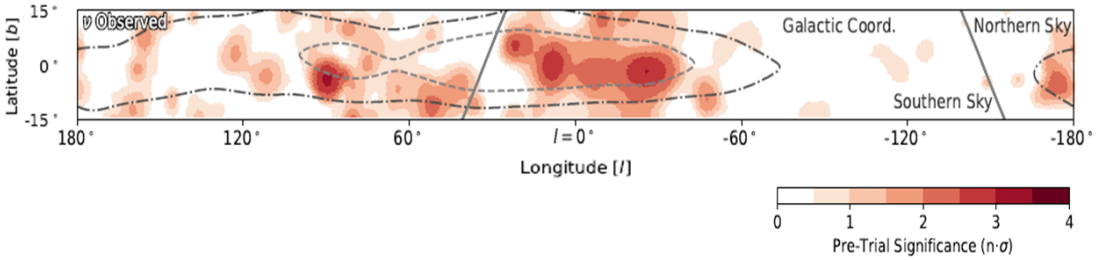

Figure 30.15: The Milky Way plane in neutrinos (Galactic coordinates, with the origin being at the Galactic Center). Shown is the pre-trial significance of the IceCube observations using a cascade neutrino event sample, calculated from an all-sky scan for point-like sources [262]. Contours indicate the regions that contain 20% and 50% of the predicted diffuse neutrino emission according to an extrapolation of Fermi-LAT results. Grey lines indicate the Northern-Southern sky horizon line.

30.4.4 *Neutrinos from astrophysical point sources*

Most point source candidates include Active Galactic Nuclei (AGN). In particular, blazars – AGN that have jets pointing towards the observer – are thought to be likely sources. In 2017, a spatial and temporal correlation was found between a flare of the electromagnetic emission from blazar TXS 0506+056 and the high-energy neutrino event IC170922A, detected by IceCube. An alert was sent to other observatories and a follow-up campaign in multiple wavelengths was started. At the moment of neutrino detection, the blazar was flaring in gamma rays, with an accidental coincidence excluded at the 3σ level [263]. Subsequent analyses of archival data revealed an excess in neutrino events with a significance of 3.5σ with respect to the expected atmospheric background, coincident with the position of TXS 0506+056, albeit not correlated with an electromagnetic flare [264].

In another analysis, the positions of 110 gamma-ray sources selected a priori were analyzed individually for a possible surplus of neutrinos over atmospheric and cosmic background expectations. An excess of 79^{+22}_{-20} neutrinos was found in the direction of the nearby AGN NGC 1068 (not a blazar, but a Seyfert-2 galaxy), at a significance of 4.2σ (see figure 30.16). The excess is spatially consistent with the direction of the strongest clustering of neutrinos in the Northern sky. The inferred flux exceeds the potential TeV gamma-ray flux by at least an order of magnitude [265], suggesting that the sight to the gamma-ray generation region is obscured, as expected for Seyfert-2 galaxies.

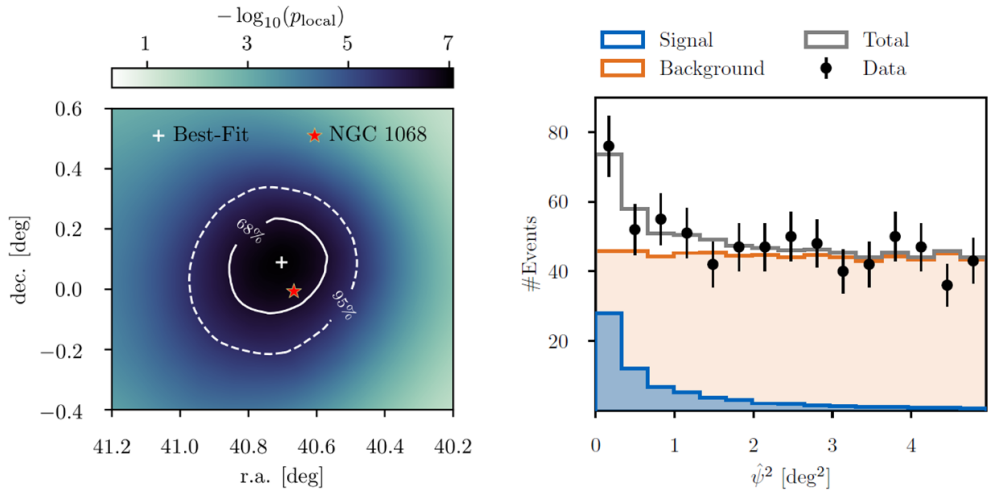

Figure 30.16: Left: The sky region around the most significant spot in the Northern Hemisphere and NGC 1068. Shown is a fine scan of the region around the hottest spot, marked by a white cross. The red circle shows the position of NGC 1068. The solid and dashed contours show the 68% and 95% confidence regions of the hot spot localization. Right: Distribution of the squared angular distance between NGC 1068 and the reconstructed event direction. Figures taken from [265].

Other potential sources include starburst galaxies, galaxy clusters, supernovae remnants (steady emission) as well as Gamma Ray Bursts (GRBs) and Tidal Disruption Events, TDEs (transient emission). Indeed, using data from IceCube and the Zwicky Transient Facility ZTF, hints for a correlation of high-energy muon neutrinos with TDEs have been reported [266].

30.4.5 *Results on particle physics*

Investigating the attenuation of high-energy neutrinos as a function of energy and their path length through the Earth, the first measurement of the neutrino-nucleon cross section at energies between a few tens of TeV and ≈ 1 PeV (corresponding to center-of-mass energies between a few

100 GeV and about 1.4 TeV) has been achieved [267], giving access in deep-inelastic scattering in a kinematic region currently not accessible to accelerator-based experiments.

The study of atmospheric high-energy neutrinos allows for the investigation of oscillation physics (see Sect. 14) at higher energies and over longer baselines than Earth-bound experiments. Constraints ($\sin^2\theta_{23} = 0.51 \pm 0.050$ and $\Delta m^2_{32} = (2.41 \pm 0.07) \times 10^{-3}\,\mathrm{eV}^2$) have been obtained with IceCube and are compatible with corresponding results from accelerator experiments [268]. Both IceCube and KM3NeT/ORCA are also sensitive to ν_τ appearance [269]. The KM3NeT/ORCA detector (under construction, see Sect. 36.3.2) is furthermore expected to provide sensitivity to the neutrino mass hierarchy.

Also, Beyond-Standard-Model (BSM) physics is being tested. For instance, constraints by IceCube on 2/4 mixing (the fourth state being a sterile neutrino) are comparable to constraints from accelerator experiments [270]. Neutrinos may have BSM interactions, and if the coupling strengths are weak or if heavy mediators are involved, these interactions may only manifest themselves in the HE and UHE neutrino sector. Corresponding constraints from IceCube have been published in [271]. Also, possible oscillation-like effects induced by quantum gravity are investigated [272].

Acknowledgement Many thanks to team members, Prof. Q. Yuan, R.Z. Yang, J. Li, X.Y. Wang, S.Z. Chen and Dr. S.Q. Xi, L. Nie, R.F. Xu, who made substantial contributions to the γ-ray part of this section. We are grateful to C. Haack and L. Schumacher for their invaluable help in producing Fig. 30.13.

References

[1] S. Abdollahi *et al.* (Fermi-LAT), Astrophys. J. Supp. **260**, 2, 53 (2022), [arXiv:2201.11184].

[2] S. P. Wakely and D. Horan, in "30th Int. Cosmic Ray Conf.", volume 3, 1341–1344 (2007).

[3] Z. Cao *et al.* (LHAASO) (2023), [arXiv:2305.17030].

[4] T. K. Gaisser, R. Engel and E. Resconi, *Cosmic Rays and Particle Physics: 2nd Edition*, Cambridge University Press (2016), ISBN 978-0-521-01646-9.

[5] Y. S. Yoon *et al.*, Astrophys. J. **728**, 122 (2011), [arXiv:1102.2575].

[6] O. Adriani *et al.* (PAMELA), Science **332**, 69 (2011), [arXiv:1103.4055].

[7] O. Adriani *et al.*, Adv. Space Res. **51**, 219 (2013).

[8] Y. S. Yoon *et al.*, Astrophys. J. **839**, 1, 5 (2017), [arXiv:1704.02512].

[9] N. Gorbunov *et al.*, Adv. Space Res. **64**, 12, 2546 (2019), [arXiv:1809.05333].

[10] M. G. Aartsen *et al.* (IceCube), Phys. Rev. D **100**, 8, 082002 (2019), [arXiv:1906.04317].

[11] Q. An *et al.* (DAMPE), Sci. Adv. **5**, 9, eaax3793 (2019), [arXiv:1909.12860].

[12] M. Aguilar *et al.* (AMS), Phys. Rept. **894**, 1 (2021).

[13] G. H. Choi *et al.*, Astrophys. J. **940**, 2, 107 (2022).

[14] O. Adriani *et al.* (CALET), Phys. Rev. Lett. **129**, 10, 101102 (2022), [arXiv:2209.01302].

[15] F. Alemanno *et al.*, Phys. Rev. Lett. **126**, 201102 (2021), [arXiv:2105.09073].

[16] H. S. Ahn *et al.*, Astrophys. J. **707**, 593 (2009), [arXiv:0911.1889].

[17] O. Adriani *et al.*, Phys. Rev. Lett. **125**, 251102 (2020), [arXiv:2012.10319].

[18] F. Aharonian *et al.* (H.E.S.S.), Phys. Rev. D **75**, 042004 (2007), [arXiv:astro-ph/0701766].

[19] M. Aguilar *et al.* (AMS), Phys. Rev. Lett. **126**, 4, 041104 (2021).

[20] O. Adriani *et al.* (CALET), Phys. Rev. Lett. **126**, 24, 241101 (2021), [arXiv:2106.08036].

[21] G. Ambrosi *et al.* (DAMPE), Nature **552**, 63 (2017), [arXiv:1711.10981].

[22] S. Abdollahi *et al.* (Fermi-LAT), Phys. Rev. D **95**, 8, 082007 (2017), [arXiv:1704.07195].

[23] O. Adriani *et al.*, Phys. Rev. Lett. **120**, 26, 261102 (2018), [arXiv:1806.09728].

[24] T. Antoni *et al.* (KASCADE), Astropart. Phys. **24**, 1 (2005), [arXiv:astro-ph/0505413].

[25] M. G. Aartsen *et al.* (IceCube), Phys. Rev. D **88**, 4, 042004 (2013), [arXiv:1307.3795].

[26] V. V. Prosin *et al.*, Nucl. Instrum. Meth. A **756**, 94 (2014).

[27] S. Schoo *et al.* (KASCADE-Grande), PoS **ICRC2015**, 263 (2016).

[28] K. Rawlins and T. Feusels (IceCube), PoS **ICRC2015**, 334 (2016).

[29] D. Ivanov, PoS **ICRC2015**, 349 (2016).

[30] A. Aab *et al.* (Pierre Auger), in "34th Int. Cosmic Ray Conf.", (2015), [arXiv:1509.03732].

[31] R. Alfaro *et al.* (HAWC), Phys. Rev. D **96**, 12, 122001 (2017), [arXiv:1710.00890].

[32] M. G. Aartsen *et al.* (IceCube), Phys. Rev. D **102**, 122001 (2020), [arXiv:2006.05215].

[33] P. Abreu *et al.* (Pierre Auger), Eur. Phys. J. C **81**, 11, 966 (2021), [arXiv:2109.13400].

[34] J. A. Morales-Soto *et al.* (HAWC), PoS **ICRC2021**, 330 (2021), [arXiv:2108.04748].

[35] D. Maurin *et al.* (2023), [arXiv:2306.08901].

[36] M. Ackermann *et al.* (Fermi-LAT), Astrophys. J. **750**, 3 (2012), [arXiv:1202.4039].

[37] Z. Cao *et al.* (LHAASO) (2023), [arXiv:2305.05372].

[38] M. Ackermann *et al.* (Fermi-LAT), Astrophys. J. **799**, 86 (2015), [arXiv:1410.3696].

[39] R. Abbasi *et al.* (IceCube), PoS **ICRC2023**, 1064 (2023).

[40] P. Sreekumar *et al.*, Phys. Rev. Lett. **70**, 127 (1993).

[41] W. Baade and F. Zwicky, Proceedings of the National Academy of Science **20**, 259 (1934).

[42] D. Ter Haar, Reviews of Modern Physics **22**, 119 (1950).

[43] L. O. Drury, Rept. Prog. Phys. **46**, 973 (1983).

[44] C. J. Cesarsky and T. Montmerle, Space Sci. Rev. **36**, 2, 173 (1983).

[45] A. M. Bykov, Astron. Astrophys. Rev. **22**, 1, 77 (2014), [arXiv:1511.04608].

[46] V. Bosch-Ramon, F. A. Aharonian and J. M. Paredes, Astron. Astrophys. **432**, 609 (2005), [arXiv:astro-ph/0411508].

[47] V. S. Ptuskin and Y. M. Khazan, Soviet Astronomy **25**, 547 (1981).

[48] F. M. Rieger, Universe **8**, 11, 607 (2022), [arXiv:2211.12202].

[49] M. Milgrom and V. Usov, Astrophys. J. Lett. **449**, L37 (1995), [arXiv:astro-ph/9505009].

[50] L. A. Anchordoqui, G. E. Romero and J. A. Combi, Phys. Rev. D **60**, 103001 (1999), [arXiv:astro-ph/9903145].

[51] G. E. Romero, A. L. Müller and M. Roth, Astron. Astrophys. **616**, A57 (2018), [arXiv:1801.06483].

[52] P. Blasi, R. I. Epstein and A. V. Olinto, Astrophys. J. **533**, L123 (2000), [arXiv:astro-ph/9912240].

[53] J. Arons, Astrophys. J. **589**, 871 (2003), [arXiv:astro-ph/0208444].

[54] V. Petrosian, Space Sci. Rev. **173**, 535 (2012), [arXiv:1205.2136].

[55] E. G. Zweibel and M. Yamada, ARA&A **47**, 1, 291 (2009).

[56] A. M. Hillas, Ann. Rev. Astron. Astrophys. **22**, 425 (1984).

[57] J. R. Jokipii, Astrophys. J. **146**, 480 (1966).

[58] K. Lodders, Astrophys. J. **591**, 1220 (2003).

[59] G. B. Rybicki, *Radiative Processes in Astrophysics*, Wiley-VCH (2004), ISBN 978-0-471-82759-7, 978-3-527-61817-0.

[60] K. Mannheim and R. Schlickeiser, Astron. Astrophys. **286**, 983 (1994), [arXiv:astro-ph/9402042].

[61] Y. Genolini *et al.*, Phys. Rev. C **98**, 3, 034611 (2018), [arXiv:1803.04686].

[62] V. L. Ginzburg and S. I. Syrovatskii, *The Origin of Cosmic Rays*, Pergamon Press (1964).

[63] E. N. Parker, Planet. Space Sci. **13**, 1, 9 (1965).

[64] A. E. Vladimirov *et al.*, Comput. Phys. Commun. **182**, 1156 (2011), [arXiv:1008.3642].

[65] C. Evoli *et al.*, JCAP **10**, 018 (2008), [Erratum: JCAP 04, E01 (2016)], [arXiv:0807.4730].

[66] R. Kissmann, Astropart. Phys. **55**, 37 (2014), [arXiv:1401.4035].

[67] D. Maurin, Comput. Phys. Commun. **247**, 106942 (2020), [arXiv:1807.02968].

[68] K. Greisen, Phys. Rev. Lett. **16**, 748 (1966).

[69] G. T. Zatsepin and V. A. Kuzmin, JETP Lett. **4**, 78 (1966).

[70] R. Kulsrud and W. P. Pearce, Astrophys. J. **156**, 445 (1969).

[71] A. R. Bell and S. G. Lucek, Mon. Not. Roy. Astron. Soc. **321**, 3, 433 (2001).

[72] C. Evoli *et al.*, Phys. Rev. Lett. **121**, 2, 021102 (2018), [arXiv:1806.04153].

[73] J. Silk and M. Srednicki, Phys. Rev. Lett. **53**, 624 (1984).

[74] F. Donato, N. Fornengo and P. Salati, Phys. Rev. D **62**, 043003 (2000), [hep-ph/9904481].

[75] S. Murgia, Ann. Rev. Nucl. Part. Sci. **70**, 455 (2020).

[76] G. Steigman, Ann. Rev. Astron. Astrophys. **14**, 339 (1976).

[77] M. Aguilar *et al.* (AMS), Phys. Rev. Lett. **124**, 21, 211102 (2020).

[78] M. Aguilar *et al.* (AMS), Phys. Rev. Lett. **126**, 8, 081102 (2021).

[79] M. Aguilar *et al.* (AMS), Phys. Rev. Lett. **127**, 2, 02101 (2021), [Erratum: Phys.Rev.Lett. 127, 159901 (2021)].

[80] O. Adriani *et al.* (CALET), Phys. Rev. Lett. **130**, 17, 171002 (2023), [arXiv:2304.14699].

[81] O. Adriani *et al.* (CALET), Phys. Rev. Lett. **129**, 25, 251103 (2022), [arXiv:2212.07873].

[82] O. Adriani *et al.*, Astrophys. J. **791**, 2, 93 (2014), [arXiv:1407.1657].

[83] J. W. Mitchell and T. Hams, *Astrophysics and Space Instrumentation*, 559–592 (2012).

[84] D. V. Reames, Lect. Notes Phys. **978**, pp. (2021), [arXiv:2010.08517].

[85] R. Engel, *Indirect Detection of Cosmic Rays*, 593–632 (2012).

[86] A. D. Panov *et al.*, Bull. Russ. Acad. Sci. Phys. **71**, 494 (2007), [arXiv:astro-ph/0612377].

[87] H. S. Ahn *et al.*, Astrophys. J. Lett. **714**, L89 (2010), [arXiv:1004.1123].

[88] F. Alemanno *et al.* (DAMPE) (2023), [arXiv:2304.00137].

[89] B. Schroer, C. Evoli and P. Blasi, Phys. Rev. D **103**, 123010 (2021), [arXiv:2102.12576].

[90] K. A. Lave *et al.*, Astrophys. J. **770**, 2, 117 (2013).

[91] J. J. Engelmann *et al.*, Astron. Astrophys. **233**, 96 (1990).

[92] M. Aguilar *et al.* (AMS), Phys. Rev. Lett. **120**, 2, 021101 (2018).

[93] A. E. Vladimirov *et al.*, Astrophys. J. **752**, 68 (2012), [arXiv:1108.1023].

[94] P. Blasi, E. Amato and P. D. Serpico, Phys. Rev. Lett. **109**, 061101 (2012), [arXiv:1207.3706].

[95] M. J. Boschini *et al.*, Astrophys. J. **889**, 167 (2020), [arXiv:1911.03108].

[96] F. Aharonian *et al.* (H.E.S.S.), Phys. Rev. Lett. **101**, 261104 (2008), [arXiv:0811.3894].

[97] O. Adriani *et al.* (PAMELA), Phys. Rev. Lett. **111**, 081102 (2013), [arXiv:1308.0133].

[98] O. Adriani *et al.* (PAMELA), Nature **458**, 607 (2009), [arXiv:0810.4995].

[99] M. Klasen, M. Pohl and G. Sigl, Prog. Part. Nucl. Phys. **85**, 1 (2015), [arXiv:1507.03800].

[100] F. A. Aharonian, A. M. Atoyan and H. J. Volk, Astron. Astrophys. **294**, L41 (1995).

[101] A. U. Abeysekara *et al.* (HAWC), Science **358**, 6365, 911 (2017), [arXiv:1711.06223].

[102] P. Blasi, Phys. Rev. Lett. **103**, 051104 (2009), [arXiv:0903.2794].

[103] P. Mertsch, A. Vittino and S. Sarkar, Phys. Rev. D **104**, 103029 (2021), [arXiv:2012.12853].

[104] C. Evoli *et al.*, Phys. Rev. D **103**, 8, 083010 (2021), [arXiv:2010.11955].

[105] P. Mertsch, JCAP **11**, 045 (2018), [arXiv:1809.05104].

[106] O. Adriani *et al.*, Pisma Zh. Eksp. Teor. Fiz. **96**, 693 (2012).

[107] G. Jóhannesson *et al.*, Astrophys. J. **824**, 1, 16 (2016), [arXiv:1602.02243].

[108] P. Blasi and P. D. Serpico, Phys. Rev. Lett. **103**, 081103 (2009), [arXiv:0904.0871].

[109] V. Poulin *et al.*, Phys. Rev. D **99**, 2, 023016 (2019), [arXiv:1808.08961].

[110] H. Fuke *et al.*, Phys. Rev. Lett. **95**, 081101 (2005), [arXiv:astro-ph/0504361].

[111] A. H. Compton and I. A. Getting, Phys. Rev. **47**, 11, 817 (1935).

[112] L. J. Gleeson and W. I. Axford, Astrophys. Sp. Sc. **2**, 4, 431 (1968).

[113] M. Aglietta *et al.* (EAS-TOP), Astrophys. J. **470**, 501 (1996).

[114] M. Ahlers and P. Mertsch, Prog. Part. Nucl. Phys. **94**, 184 (2017), [arXiv:1612.01873].

[115] A. Abdul Halim *et al.* (Pierre Auger), Astrophys. J. Suppl. **264**, 2, 50 (2023), [arXiv:2211.16020].

[116] R. U. Abbasi *et al.* (Telescope Array), Science **382**, 6673, abo5095 (2023), [arXiv:2311.14231].

[117] S. Sciutto, AIRES User's Manual and Reference Guide; version 19.04.00`http://aires.fisica.unlp.edu.ar/`.

[118] A. Aab *et al.* (Pierre Auger), Phys. Rev. D **100**, 8, 082003 (2019), [arXiv:1901.08040].

[119] D. Heck and T. Pierog, Extensive Air Shower Simulation with CORSIKA: A User's Guide (Version 7.7420)`https://www.iap.kit.edu/corsika/70.php`.

[120] F. Riehn *et al.*, Phys. Rev. D **102**, 6, 063002 (2020), [arXiv:1912.03300].

[121] S. Ostapchenko, EPJ Web Conf. **208**, 11001 (2019).

[122] T. Pierog *et al.*, Phys. Rev. C **92**, 3, 034906 (2015), [arXiv:1306.0121].

[123] W. Heitler, *The quantum theory of radiation*, volume 5 of *International Series of Monographs on Physics*, Oxford University Press, Oxford (1936).

[124] J. Matthews, Astropart. Phys. **22**, 387 (2005).

[125] A. Aab *et al.* (Pierre Auger), Nucl. Instrum. Meth. A **798**, 172 (2015), [arXiv:1502.01323].

[126] H. Kawai *et al.* (Telescope Array), Nucl. Phys. B Proc. Suppl. **175-176**, 221 (2008).

[127] S. Knurenko and I. Petrov, Adv. Space Res. **64**, 12, 2570 (2019), [arXiv:1908.01508].

[128] N. M. Budnev *et al.*, Astropart. Phys. **117**, 102406 (2020), [arXiv:2104.03599].

[129] A. Aab *et al.* (Pierre Auger), Phys. Rev. Lett. **116**, 24, 241101 (2016), [arXiv:1605.02564].

[130] J. Pawlowski (Pierre Auger), PoS **ICRC2023**, 016 (2023), [arXiv:2312.14673].

[131] P. A. Bezyazeekov *et al.*, Phys. Rev. D **97**, 12, 122004 (2018), [arXiv:1803.06862].

[132] I. Petrov and S. Knurenko, PoS **ICRC2019**, 385 (2020).
[133] P. Schellart *et al.*, Astron. Astrophys. **560**, A98 (2013), [arXiv:1311.1399].
[134] S. Buitink *et al.*, PoS **ICRC2023**, 503 (2023).
[135] A. Aab *et al.* (Pierre Auger) (2016), [arXiv:1604.03637].
[136] E. Kido (Telescope Array), EPJ Web Conf. **210**, 06001 (2019).
[137] M. G. Aartsen *et al.* (IceCube) (2014), [arXiv:1412.5106].
[138] J. Álvarez-Muñiz *et al.* (GRAND), Sci. China Phys. Mech. Astron. **63**, 1, 219501 (2020), [arXiv:1810.09994].
[139] D. Southall *et al.*, Nucl. Instrum. Meth. A **1048**, 167889 (2023), [arXiv:2206.09660].
[140] D. Ivanov (Telescope Array), PoS **ICRC2019**, 298 (2020).
[141] A. Aab *et al.* (Pierre Auger), Phys. Rev. D **102**, 6, 062005 (2020), [arXiv:2008.06486].
[142] A. Coleman *et al.*, Astropart. Phys. **149**, 102819 (2023), [arXiv:2205.05845].
[143] R. U. Abbasi *et al.* (Telescope Array), Astrophys. J. **858**, 2, 76 (2018), [arXiv:1801.09784].
[144] R. U. Abbasi *et al.* (Telescope Array), Astrophys. J. **909**, 2, 178 (2021), [arXiv:2012.10372].
[145] A. Yushkov (Pierre Auger), PoS **ICRC2019**, 482 (2020).
[146] C. J. Todero Peixoto (Pierre Auger), PoS **ICRC2019**, 440 (2020).
[147] N. M. Budnev *et al.* (TAIGA), PoS **ICRC2021**, 731 (2021).
[148] A. Fedynitch *et al.*, Phys. Rev. D **100**, 10, 103018 (2019), [arXiv:1806.04140].
[149] A. Abdul Halim *et al.* (Pierre Auger), Phys. Rev. Lett. **132**, 2, 021001 (2024), [arXiv:2310.19963].
[150] A. A. Watson, JHEAp **33**, 14 (2022), [arXiv:2112.06525].
[151] A. Aab *et al.* (Pierre Auger), JINST **16**, 07, P07019 (2021), [arXiv:2101.02946].
[152] F. G. Schröder, Prog. Part. Nucl. Phys. **93**, 1 (2017), [arXiv:1607.08781].
[153] D. Hooper, S. Sarkar and A. M. Taylor, Astropart. Phys. **27**, 199 (2007), [arXiv:astro-ph/0608085].
[154] G. Golup *et al.* (Pierre Auger), PoS **ICRC2023**, 252 (2023).
[155] J. Kim *et al.* (Telescope Array), PoS **ICRC2023**, 244 (2023).
[156] A. Aab *et al.* (Pierre Auger), Front. Astron. Space Sci. **6**, 24 (2019), [arXiv:1904.11918].
[157] B. P. Abbott *et al.*, Astrophys. J. Lett. **848**, 2, L12 (2017), [arXiv:1710.05833].
[158] A. Albert *et al.*, Astrophys. J. Lett. **850**, 2, L35 (2017), [arXiv:1710.05839].
[159] S. Mollerach and E. Roulet, JCAP **03**, 017 (2019), [arXiv:1812.04026].
[160] A. A. Halim *et al.* (Pierre Auger), JCAP **05**, 024 (2023), [arXiv:2211.02857].
[161] J. C. Arteaga Velazquez, PoS **ICRC2023**, 466 (2023).
[162] A. Aab *et al.* (Pierre Auger), Phys. Rev. Lett. **126**, 15, 152002 (2021), [arXiv:2102.07797].
[163] M. Tavani *et al.* (AGILE), Astron. Astrophys. **502**, 995 (2009), [arXiv:0807.4254].
[164] J. Chang *et al.* (DAMPE), Astropart. Phys. **95**, 6 (2017).
[165] S. Torii, C. Collaboration *et al.*, J. Jpn. Soc. Microgravity Appl. **24**, 1, 120 (2007).
[166] W. B. Atwood *et al.* (Fermi-LAT), Astrophys. J. **697**, 1071 (2009).
[167] F. Aharonian *et al.* (H.E.S.S.), Astron. Astrophys. **457**, 899 (2006), [arXiv:astro-ph/0607333].
[168] J. Sitarek *et al.* (MAGIC), in "33rd Int. Cosmic Ray Conf.", 0074 (2013), [arXiv:1308.0141].

[169] D. B. Kieda (VERITAS), in "33rd Int. Cosmic Ray Conf.", 0700 (2013), [arXiv:1308.4849].
[170] F. Di Pierro (CTA LST Project), J. Phys. Conf. Ser. **2429**, 1, 012020 (2023).
[171] A. Abramowski *et al.* (H.E.S.S.), Phys. Rev. D **90**, 12, 122007 (2014).
[172] N. Budnev *et al.*, Nucl. Instrum. Meth. A **958**, 162113 (2020).
[173] G. Aielli *et al.*, Nucl. Instrum. Meth. A **661**, S50 (2012).
[174] M. Takita *et al.* (TIBET ASγ), in "30th Int. Cosmic Ray Conf.", volume 2, 575–578 (2007).
[175] B. M. Baughman, in "32nd Int. Cosmic Ray Conf.", volume 9, 123 (2011).
[176] Z. Cao, Nature Astron. **5**, 8, 849 (2021).
[177] J. A. Hinton (H.E.S.S.), New Astron. Rev. **48**, 331 (2004).
[178] C. Baixeras, Nuclear Physics B - Proceedings Supplements **114**, 247 (2003), ISSN 0920-5632.
[179] H. B. T.C Weekes *et al.*, Astroparticle Physics **17**, 2, 221 (2002), ISSN 0927-6505.
[180] G. W. Clark *et al.*, Astrophysical Journal, Letters **153**, L203 (1968).
[181] C. E. Fichtel *et al.*, Astrophysical Journal **198**, 163 (1975).
[182] H. A. Mayer-Hasselwander *et al.*, Astronomy and Astrophysics **105**, 1, 164 (1982).
[183] S. D. Hunter *et al.*, Astrophys. J. **481**, 205 (1997).
[184] M. Ackermann *et al.*, The Astrophysical Journal **750**, 1, 3 (2012).
[185] A. A. Abdo *et al.*, Astrophys. J. **688**, 1078 (2008).
[186] B. Bartoli *et al.* (ARGO-YBJ), Astrophys. J. **806**, 20 (2015).
[187] M. Amenomori *et al.* (Tibet ASgamma), Phys. Rev. Lett. **126**, 14, 141101 (2021).
[188] P. Sreekumar *et al.* (EGRET), Astrophys. J. **494**, 523 (1998).
[189] M. Ackermann *et al.* (Fermi-LAT), Astrophys. J. **799**, 86 (2015).
[190] Z. Cao *et al.*, Annual Review of Nuclear and Particle Science **73**, in press, 341 (2023).
[191] S. Funk, Ann. Rev. Nucl. Part. Sci. **65**, 245 (2015).
[192] J. A. Hinton and W. Hofmann, Ann. Rev. Astron. Astrophys. **47**, 523 (2009), [arXiv:1006.5210].
[193] V. Schoenfelder (COMPTEL), Astron. Astrophys. Suppl. Ser. **143**, 145 (2000), [arXiv:astro-ph/0002366].
[194] S. Abdollahi *et al.* (Fermi-LAT), Astrophys. J. Suppl. **247**, 1, 33 (2020).
[195] Z. Cao *et al.* (LHAASO), Science **373**, 6553, 425 (2021).
[196] F. A. Aharonian *et al.* (H.E.S.S.), Nature **432**, 75 (2004).
[197] M. C. Weisskopf *et al.*, Astrophys. J. Lett. **536**, L81 (2000).
[198] F. Aharonian (H.E.S.S.), Astron. Astrophys. **464**, 235 (2007).
[199] H. Abdalla *et al.* (H.E.S.S.), Astron. Astrophys. **612**, A6 (2018).
[200] R. Bühler and R. Blandford, Rept. Prog. Phys. **77**, 066901 (2014).
[201] A. A. Abdo *et al.*, Science **326**, 5959, 1512 (2009).
[202] J. Li *et al.*, Nature Astron. **4**, 12, 1177 (2020).
[203] R. Zanin *et al.*, Astron. Astrophys. **596**, A55 (2016), [arXiv:1605.05914].
[204] J. Albert *et al.* (MAGIC), Astrophys. J. Lett. **665**, L51 (2007).
[205] G. Martí-Devesa and O. Reimer, Astron. Astrophys. **654**, A44 (2021).
[206] A. A. Abdo *et al.*, VizieR Online Data Catalog J/ApJS/208/17 (2013).

[207] S. Ansoldi *et al.* (MAGIC), Astron. Astrophys. **585**, A133 (2016), [arXiv:1510.07048].
[208] A. Djannati-Ataï, in "31st Texas Symposium on Relativistic Astrophysics," 33 (2022).
[209] A. Allafort *et al.* (Fermi-LAT), Astrophys. J. Lett. **777**, L2 (2013).
[210] A. A. Abdo *et al.* (Fermi-LAT), Astrophys. J. Suppl. **208**, 17 (2013).
[211] H. An, Astrophys. J. **924**, 2, 91 (2022).
[212] C. J. Clark *et al.*, Nature Astron. **7**, 4, 451 (2023).
[213] D. F. Torres *et al.*, Astrophys. J. **836**, 1, 68 (2017).
[214] A. Franckowiak *et al.*, Astron. Astrophys. **609**, A120 (2018).
[215] S. De Wolf *et al.* (H.E.S.S.), Science **376**, 6588, abn0567 (2022).
[216] M. Ajello *et al.* (Fermi-LAT), Astrophys. J. **892**, 105 (2020).
[217] M. Ajello *et al.* (Fermi-LAT), Astrophys. J. Suppl. **263**, 2, 24 (2022).
[218] M. Hayashida *et al.*, Astrophys. J. **807**, 1, 79 (2015).
[219] V. A. Acciari *et al.*, Astrophys. J. **738**, 25 (2011), [arXiv:1106.1210].
[220] M. Sikora, M. C. Begelman and M. J. Rees, Astrophys. J. **421**, 153 (1994).
[221] F. A. Aharonian, New Astron. **5**, 377 (2000).
[222] B. Bartoli *et al.* (ARGO-YBJ), Astrophys. J. **734**, 110 (2011).
[223] B. Bartoli, r. Xu *et al.* (ARGO-YBJ), Astrophys. J. **758**, 2 (2012).
[224] B. Bartoli *et al.* (ARGO-YBJ), Astrophys. J. Suppl. **222**, 1, 6 (2016).
[225] A. Albert *et al.* (HAWC), Astrophys. J. **929**, 2, 125 (2022).
[226] K. Katarzynski *et al.*, Astron. Astrophys. **433**, 479 (2005), [arXiv:astro-ph/0412405].
[227] Z.-H. An *et al.* (Insight-HXMT, GECAM) (2023), [arXiv:2303.01203].
[228] Z. Cao *et al.* (LHAASO), Science **380**, 6652, 9328 (2023).
[229] V. A. Acciari *et al.* (MAGIC), Nature **575**, 7783, 459 (2019).
[230] H. Abdalla *et al.*, Nature **575**, 7783, 464 (2019).
[231] M. Ajello *et al.*, Astrophys. J. **878**, 1, 52 (2019).
[232] P. Kumar and R. B. Duran, Mon. Not. Roy. Astron. Soc. **400**, 75 (2009).
[233] X.-Y. Wang *et al.*, Astrophys. J. **712**, 1232 (2010).
[234] V. A. Acciari *et al.* (MAGIC), Nature **575**, 7783, 455 (2019).
[235] H. Abdalla *et al.* (H.E.S.S.), Science **372**, 6546, 1081 (2021).
[236] S. R. Coleman and S. L. Glashow, Phys. Rev. D **59**, 116008 (1999), [hep-ph/9812418].
[237] F. W. Stecker and S. L. Glashow, Astropart. Phys. **16**, 97 (2001), [arXiv:astro-ph/0102226].
[238] Z. Cao *et al.* (LHAASO), Phys. Rev. Lett. **128**, 5, 051102 (2022).
[239] R. Abbasi *et al.* (IceCube), Eur. Phys. J. C **82**, 11, 1031 (2022), [arXiv:2011.03561].
[240] R. Mammen Abraham *et al.*, J. Phys. G **49**, 11, 110501 (2022), [arXiv:2203.05591].
[241] J. Abraham *et al.* (Pierre Auger), Phys. Rev. Lett. **100**, 211101 (2008), [arXiv:0712.1909].
[242] S. Ostapchenko, M. V. Garzelli and G. Sigl, Phys. Rev. D **107**, 2, 023014 (2023), [arXiv:2208.12185].
[243] E. Richard *et al.* (Super-Kamiokande), Phys. Rev. D **94**, 052001 (2016), [arXiv:1510.08127].
[244] S. Adrian-Martinez *et al.* (ANTARES), Eur. Phys. J. C **73**, 2606 (2013), [arXiv:1308.1599].

[245] M. G. Aartsen *et al.* (IceCube), Phys. Rev. D **91**, 122004 (2015), [arXiv:1504.03753].

[246] M. Börner *et al.* (IceCube), PoS **ICRC2015**, 1098 (2016).

[247] M. Aartsen *et al.* (IceCube), Nature **591**, 220 (2021), [arXiv:2110.15051].

[248] M. G. Aartsen *et al.* (IceCube), Phys. Rev. D **98**, 6, 062003 (2018), [arXiv:1807.01820].

[249] M. Niechciol *et al.* (Pierre Auger), PoS **ICRC2023**, 1488 (2023).

[250] A. van Vliet, R. Alves Batista and J. R. Hörandel, Phys. Rev. D **100**, 2, 021302 (2019), [arXiv:1901.01899].

[251] R. Abbasi *et al.* (IceCube), Phys. Rev. D **104**, 02202 (2021), [arXiv:2011.03545].

[252] R. Abbasi *et al.* (IceCube), Astrophys. J. **928**, 50 (2022), [arXiv:2111.10299].

[253] L. A. Fusco and F. Versari (ANTARES), PoS **ICRC2019**, 891 (2020).

[254] V. Allakhverdyan *et al.* (Baikal-GVD), Phys. Rev. D **107**, 042005 (2023), [arXiv:2211.09447].

[255] S. L. Glashow, Phys. Rev. **118**, 316 (1960).

[256] D. Biehl *et al.*, JCAP **01**, 033 (2017), [arXiv:1611.07983].

[257] V. Berezinsky and G. Zatsepin, Phys. Lett. B **28**, 423 (1969).

[258] M. Ave *et al.*, Phys. Rev. Lett. **85**, 2244 (2000), [arXiv:astro-ph/0007386].

[259] D. Hooper, A. Taylor and S. Sarkar, Astropart. Phys. **23**, 11 (2005), [arXiv:astro-ph/0407618].

[260] D. Gaggero *et al.*, Phys. Rev. D **91**, 083012 (2014), [arXiv:1411.7623].

[261] A. Albert *et al.* (ANTARES), Phys. Lett. B **481**, 137951 (2023), [arXiv:2212.11876].

[262] R. Abbasi *et al.* (IceCube), Science **380**, 6652 (2023), [arXiv:2307.04427].

[263] M. Aartsen *et al.* (IceCube, Fermi-LAT, MAGIC, AGILE, ASAS-SN, HAWC, H.E.S.S., INTEGRAL, Kanata, Kiso, Kapteyn, Liverpool Telescope, Subaru, Swift NuSTAR, VERITAS, VLA/17B-403), Science **361**, eaat1378 (2018), [arXiv:1807.08816].

[264] M. Aartsen *et al.* (IceCube), Science **361**, 147 (2018), [arXiv:1807.08794].

[265] R. Abbasi *et al.* (IceCube), Science **378**, 538 (2022), [arXiv:2211.09972].

[266] R. Stein *et al.*, MNRAS **521,4**, 5046 (2023), [arXiv:2203.17135].

[267] M. G. Aartsen *et al.* (IceCube), Nature **551**, 596 (2017), [arXiv:1711.08119].

[268] R. Abbasi *et al.* (IceCube), Phys. Rev. D **108**, 1, 012014 (2023), [arXiv:2304.12236].

[269] N. Geisselbrecht (KM3NeT), PoS **ICRC2023**, 1107 (2023).

[270] M. G. Aartsen *et al.* (IceCube), Phys. Rev. Lett. **125**, 14, 141801 (2020), [arXiv:2005.12942].

[271] R. Abbasi *et al.* (IceCube), Phys. Rev. Lett. **129**, 1, 011804 (2022), [arXiv:2201.03566].

[272] A. Addazi *et al.*, Prog. Part. Nucl. Phys. **125**, 103948 (2022), [arXiv:2111.05659].